NASA CR-72344
Series 8, Issue 104

FINAL REPORT:

INVESTIGATION OF KILOVOLT ION SPUTTERING

by

HAROLD P. SMITH, JR.

prepared for

NATIONAL AERONAUTICS AND SPACE ADMINISTRATION

CONTRACT NAS 3-5743

N68-17483
(ACCESSION NUMBER) (THRU)
106 1
(PAGES) (CODE)
CR-72344 20
(NASA CR OR TMX OR AD NUMBER) (CATEGORY)
FACILITY FORM 602

GPO PRICE $ _____

CFSTI PRICE(S) $ _____

Hard copy (HC) 3.00

Microfiche (MF) .65

ff 653 July 65

SPACE SCIENCES LABORATORY
UNIVERSITY OF CALIFORNIA, BERKELEY 94720

NOTICE

This report was prepared as an account of Government sponsored work. Neither the United States, nor the National Aeronautics and Space Administration (NASA), nor any person acting on behalf of NASA:

A.) Makes any warranty or representation, expressed or implied, with respect to the accuracy, completeness, or usefulness of the information contained in this report, or that the use of any information, apparatus, method, or process disclosed in this report may not infringe privately owned rights; or

B.) Assumes any liabilities with respect to the use of, or for damages resulting from the use of any information, apparatus, method or process disclosed in this report.

As used above, "person acting on behalf of NASA" includes any employee or contractor of NASA, or employee of such contractor, to the extent that such employee or contractor of NASA, or employee of such contractor prepares, disseminates, or provides access to, any information pursuant to his employment or contract with NASA, or his employment with such contractor.

Requests for copies of this report should be referred to

National Aeronautics and Space Administration
Office of Scientific and Technical Information
Attention: AFSS-A
Washington, D.C. 20546

NASA CR-72344
Series 8, Issue 104

FINAL REPORT

INVESTIGATION OF KILOVOLT ION SPUTTERING

by

Harold P. Smith, Jr.

prepared for

NATIONAL AERONAUTICS AND SPACE ADMINISTRATION

June 30, 1967

Distribution of this report is provided in the interest of information exchange. Responsibility for the contents resides in the author or organization that prepared it.

CONTRACT NAS 3-5743

Technical Management
Nasa Lewis Research Center
Cleveland, Ohio

Spacecraft Technology Division
Mr. J. A. Wolters

SPACE SCIENCES LABORATORY
University of California, Berkeley 94720

TABLE OF CONTENTS

SUMMARY i

1. INTRODUCTION 1

2. YIELD AND ANGULAR DISTRIBUTION OF CESIUM SPUTTERED COPPER USING A RADIOACTIVE TRACER TECHNIQUE 3

2.1 Experimental Technique 3

2.2 Results and Discussion 6

2.2.1 Total Yield 6

2.2.2 Angular Distribution Measured at Normal Incidence 8

2.2.3 Angular Distribution Measured at Non-Normal Incidence 11

3. YIELD AND ANGULAR DISTRIBUTION OF CESIUM-SPUTTERED MOLYBDENUM 12

3.1 Apparatus and Experimental Procedure . 12

3.2 Results and Discussion 13

3.2.1 Yield 13

3.2.2 Angular Distribution 15

4. CESIUM ION SPUTTERING OF ALUMINUM 18

4.1 Introduction 18

4.2 Results and Discussion 21

4.2.1 Sputtering Yield 21

4.2.2 Effect of Oxygen Partial Pressure . . 23

5. CESIUM ION BOMBARDMENT OF ALUMINUM OXIDE IN A CONTROLLED OXYGEN ENVIRONMENT 25

5.1 Introduction 25

5.2 Experimental Technique 26

5.3 Results and Discussion 28

5.3.1 Effect of Ion Energy 28

5.3.2 Effect of Oxygen Partial Pressure . . 29

5.3.3 Effect of Temperature 30

6. DETERMINATION OF ANGULAR DISTRIBUTION OF CESIUM ION SPUTTERED ALUMINUM ATOMS BY ELECTRON MICROPROBE ANALYSIS 31

6.1 Introduction 31

6.2 Experimental Technique 32

6.3 Results and Discussion 33

6.4 Conclusions 34

7. MERCURY ION SPUTTERING OF Cu, Mo, and Ni . . . 35

7.1 Introduction 35

7.2 Experimental Technique 35

7.3 Results and Discussion 36

7.3.1 Yield 36

7.3.1.1 Normal Incidence 36

7.3.1.2 Oblique Incidence 37

7.3.1.3 Temperature Effects 37

7.3.2 Angular Distribution 37

7.3.2.1 Normal Incidence 37

7.3.2.2 Oblique Incidence 40

8. MEASUREMENT OF THIN OXIDE FILMS BY CHARACTERISTIC OXYGEN K-SHELL X-RAY PRODUCTION 45

8.1 Introduction 45

8.2 Experimental Apparatus and Methods . . 47

8.2.1 Vacuum Considerations 47

8.2.2 Ion Source and Beam Analysis 49

8.2.3 Target Current Measurements 50

8.2.4 Characteristic X-ray Detection 52

8.2.5 Target Preparation 55

8.3 Characteristic Aluminum K-Shell X-ray Yield Measurements 57

8.4 Characteristic Oxygen K-Shell X-ray Yield Measurements 59

8.4.1 Theory 59

8.4.2 Results 61

8.4.3 Discussion 64

FIGURES 67

TABLES 91

REFERENCES 95

DISTRIBUTION LIST 100

Summary

The yield (ejected atoms/incident ion) and the angular distribution of ejected particles (atoms $ion^{-1}sr^{-1}$) are presented and discussed for a wide variety of experimental conditions. Highly polished, monocrystalline surfaces of Cu, Mo, Ni, Al, and Al_2O_3 were bombarded by either Cs^+ or Hg^+, two ion species which find application in ion rocket propulsion. The yield and angular distribution were measured as functions of energy of the incident ion ($1 < E < 10$ keV), angle of incidence with respect to the target surface, crystallographic orientation of the target with respect to the surface and to the incident ion beam, temperature of the target, and partial pressure of oxygen. Among the major conclusions are (a) the yield can be significantly reduced by directing the incident beam along low index crystallographic directions, (b) normal incidence significantly reduces yield, (c) short term annealing is important in that the yield of refractory materials is reduced at higher temperatures; whereas, temperature has little effect on the non-refractory materials, (d) preferred emission along close-packed directions is of secondary importance in the high yield region, and (e) reactive gas film formation at the metalic surface can significantly reduce yield; thereby, showing the need for ultra high vacuum testing of ion rocket engines.

In addition to the above, a proton microprobe has been developed which is capable of detecting one-tenth monolayer coverage of oxygen on an aluminum substrate. There are many other combinations of gases and substrates that should be amenable to measurement with the described probe.

1. Introduction

The phenomenon of sputtering has been known and investigated for nearly a century; yet the mechanism and characteristics of the process are not thoroughly understood. As a result of improved techniques in high-vacuum systems and surface physics measurements, more reliable and reproducible data are becoming available. The ion rocket propulsion concept has drawn special interest to heavy ion sputtering of metals, since the major factor presently limiting the operational lifetime of deep probe electrostatic propulsion thrusters is the sputtering erosion of the accelerator electrode system by the propellant particles. By exploring the sputtering process and how it is affected by crystal orientation, surface film, and environment, to mention some of the variables of influence, it is hoped that a reduction in nuisance sputtering can be achieved. However, of equal importance is the rapid growth of useful application of ion-surface technology. Sputter cleaning of surfaces is the most widely used method for creating clean surfaces in ultra-high vacuum. Ion machining is becoming not only a reality, but a necessity in the utilization of advanced compounds in microcircuitry. Ion implantation is an integral part of ion-surface technology.

For the reasons noted above, the NASA Lewis Research Center initiated an investigation of kilovolt ion sputtering at the University of California Space Sciences Laboratory in April, 1964, under contract NAS 3 5743. This document is submitted as a final report on this work. The format follows closely the doctoral and master's theses which were partially supported by the contract.

In this sense, Section 2 is primarily the work of Dr. N.T. Olson, Section 3 - Lt (jg) J.B. Green, USN, Section 4 - Capt. A.E. Andrews, USA, Section 5 and 6 - Dr. E.H. Hasseltine, Section 7 - Dr. R.G. Musket, and Section 8 - Dr. R.R. Hart. Acknowledgement of their dedicated contributions to this work is gratefully made. Furthermore, it is a pleasure to acknowledge the continued guidance and supervision of many members of the University staff; especially Dr. F.C. Hurlbut, Dr. T.H. Pigford, Dr. J.M. Khan, and Dr. N.T. Olson.

2. Yield and Angular Distribution of Cesium Sputtered Copper Using a Radioactive Tracer Technique

2.1 Experimental Technique

Radioactive tracer techniques have been used previously in sputtering measurements. O'Brian, Lindner, and Moore,[O1] and Gronlund and Moore[G1] measured the yield of polycrystalline silver by radiation detection of the silver sputtered from a neutron activated target. Patterson and Tomlin[P1] extended this technique to measurements of the angular distribution of sputtered material from a polycrystalline target. Nelson and Thompson,[N1] in a number of excellent measurements of both yields and angular distributions, have made extensive use of neutron activation of the sputtered material rather than using a radioactive target. Since activation of the target before ion bombardment has the advantage of increased sensitivity in the case of copper and other long-lived isotopes, rather than activation of the sputtered particles (and associated collector) following ion bombardment, we have chosen to extend the former technique to single crystals for angular distribution measurements.

The experimental apparatus consists of a large target chamber evacuated by a cryogenically baffled,oil diffusion pump and an ion source chamber evacuated by a 200 l/sec vac-ion pump (Fig. 2-1). Metal gaskets are used exclusively in the target chamber, whereas viton o-rings are used for three ports on the source chamber. The base pressure of both systems was 2×10^{-8} torr without recourse to baking. During ion beam operation, the pressure was 1.5×10^{-7} torr or lower in both chambers.

A porous tungsten, surface ionization cesium ion source was operated at 1 to 10 keV and insulated from the target chamber by the glass tee. The source provided 10 to 20 μa at the target surface when used in conjunction with an alternating potential, electrostatic focusing system. Since the measured target cross section of the beam was 0.7 cm^2, sputtering took place under clean surface conditions.[Y1]

The maximum sensitivity of the radioactive tracer technique is determined by the saturation activity that can be induced in the particular material. However, the radiological hazard involved in handling the copper specimens precluded activation to saturation. The practical maximum sensitivity is thus set by the maximum activity that can be reasonably handled. Thus, the smaller the total target weight, the higher the specific activity (curies/g) and the higher the detection sensivity.

To prepare as small a target as possible, a thin wafer (0.030 in.) was spark cut from a 3/4-in.-diam single-crystal copper rod. The wafer was chemically and then electrically polished to a thickness of 0.005 in. This method of preparation leaves the crystal structure undisturbed. Following preparation, the crystallographic orientation of the target was measured by Laue-back x-ray diffraction. A high purity aluminum holder was then constructed to insure alignment of the ion beam to within 1° of the desired direction.

Neutron capture by Cu^{63} (69% abundant) produced Cu^{64}, which is positron unstable and decays with a half-life of 12.9 hr. The radioactive monocrystalline target, mounted in the collector assembly as illustrated in Fig. 2-2, was aligned with the [100]

crystallographic direction at normal incidence and the [110] or [755] at 45° incidence. The radioactivity was induced by exposing the copper target to a thermal neutron flux of 5×10^{12} neutrons cm^{-2} sec^{-1} for 15 min, thus providing sufficient activity to detect 0.1 μg of sputtered copper when measured using a NaI scintillation well crystal with multichannel spectrum analysis.

The collector, illustrated in Fig. 2-2, surrounded the entire 2π sr opposite the target so that both angular and total yield measurements were possible. To facilitate the angular distribution measurements, 2.7 sr of the collector above the target were fabricated from 100 aluminum cubes placed in a 10 x 10 array. The polar and azimuthal positions of the 25 collectors in each quadrant are given in Fig. 2-3 along with their solid angle relative to the target. The angular distribution was determined by measuring the copper radioactivity of each cube. An absolute measure was then obtained by direct comparison with the radioactivity of a copper standard of known weight irradiated at the same time and under the same conditions as the target. The sides and top portions of the collector were aluminum foil which were crushed for counting. Thus, the total yield was determined by summing the amount of copper on the 100 cubes, the side, and top foils. In principle, the top collector foil, residing in the plane of the target surface, should not have collected any sputtered copper. It did, however, collect 2 to 3% of the total. This fraction (as illustrated in Fig. 2-2) could be a result of secondary sputtering of copper already collected on the cubes or a sticking probability slightly less than unity. Whichever the case, the error in the

measured distribution is small.

The total number of ions striking the target was determined by summing and integrating the current to the target and collector assembly that serves as a simplified Faraday cage, thereby removing any inaccuracy associated with secondary and photoelectron production in the assembly. Auxillary measurements were made to insure that 1) the ion beam did not strike the collector when entering the assembly, 2) beam divergence after entering was not sufficient to spread the beam to a wider cross-sectional area than the target, 3) the ion beam was not contaminated by secondary electrons created in the lens structure by ion bombardment, and 4) negligibly few secondary electrons created at the target could escape the target collector assembly. This last consideration was determined by showing that the summed current was independent of bias voltage between the target and the collector. Furthermore, calculations based on the ion beam potential as seen by secondary electrons and solid angle considerations preclude significant error from escaping secondaries.

2.2 Results and Discussion

2.2.1 Total Yield

The total yield, $S(E,T,\alpha)$, shown in Figs. 2-4 and 2-5, as a function of ion energy E, target temperature T, and angle of incidence α, measured from the surface normal, emphasizes the importance of heavy ion "channeling"[K1,N2] in the sputtering process. Ions, incident along the open or transparent [100] axis , as was the case for the normal incidence experiments, have a smaller probability of losing energy by momentum transfer

to lattice atoms in the first few monolayers than those ions directed along randomly oriented crystallographic axes. Therefore, the sputtering yield for ion beam alignment parallel to low-index directions should be less than the yield encountered in sputtering of polycrystalline targets under the same experimental conditions. Furthermore, the yield as a function of incident ion energy is expected to reach a maximum and to decrease as the energy of the ion is increased since the effective radius of interaction for momentum transfer to the lattice atoms also decreases, thus enhancing the channeling process and reducing the magnitude of the total yield. Alignment of the ion beam with those crystallographic directions that enhance channeling should then reduce the energy at which the maximum occurs.

Comparison of the data presented in Fig. 2-4 with those of Almen and Bruce,[A1] who report a xenon-polycrystalline copper yield of 10 atoms per ion at 10 keV, whereas we report 6, substantiates the contention of reduced yield for low-index alignment. The same reference also shows that $(\partial S/\partial E)_{E=10\ \mathrm{keV}} > 0$ for a polycrystalline target, whereas a broad plateau, $(\partial S/\partial E)_{E>5\ \mathrm{keV}} \simeq 0$ can be discerned in our monocrystalline copper yield curve of Fig. 2-4.[F1,S5,S6]

Similar conclusions can be drawn with regard to measurements at $\alpha = 45°$. Since non-normal incidence decreases ion penetration normal to the surface of the lattice without significantly affecting total momentum transfer per collision, the S(E) curve at $\alpha = 45°$ is expected to be higher than that at 0°, as is the case shown in Fig. 2-5.[S1] The effect of ion penetration is further emphasized by the large increase in yield for bombardment along the opaque [755] as opposed to the transparent [110] direction.

The high-yield, high-index results are similar to the data of Magnuson et al.,[M1] who report a monotonically increasing S(E) curve for argon-ion bombardment of the (110) face of copper parallel to the [111] direction, which is relatively opaque in the fcc system despite the low value of the Miller indices.

Target temperature variation from 77 to 473°K had no measurable effect on total yield. If it is contended that the primary effect of target temperature on sputtering is annealing of the ion-bombardment induced, radiation damage,[G2] then the effect of the above temperature variation should be small since radiation damage studies indicate that rapid annealing occurs in copper for temperature greater than 100°K.[C1,C2]

2.2.2 Angular Distribution Measured at Normal Incidence

The angular distribution is reported as the fractional yield per unit fractional solid angle, $(\Delta S_i/S)/(\Delta\Omega_i/2\pi)$, where ΔS_i is the yield on and $\Delta\Omega_i$ is the solid angle subtended by the ith collector. A nonlinear regression analysis of the 100, four-fold symmetric, angular data points, normalized to isotropic emission, was made in order to express the data in analytic form.

$$\frac{2\pi}{S}\frac{dS}{d\Omega}(\theta,\phi) = B_1 \cos\theta + B_2 \exp\left\{-(2\sigma^2)^{-1}[(\theta_1-\theta)^2 + (\phi_1-\phi)^2 \sin^2\theta_1]\right\}, \qquad (2\text{-}1)$$

where

$$S = \int_{2\pi} d\Omega(\theta,\phi)\ (dS/d\Omega)$$

and θ and ϕ are the polar and azimuthal angles. The values of θ_1 and ϕ_1 were determined by the orientation of the [110] crystallographic direction with respect to the collector, while B_1, B_2, and σ were adjusted by regression analysis to yield minimum (square) error between the analytic function and the 100 data. A second regression analysis, in which θ_1 and ϕ_1 were adjusted rather than predetermined by the [110] orientation, had no significant effect.

The Gaussian functions, centered about the closepacked directions, were chosen for their convenience in representing "Wehner spots"[W1] and because of the similarity of the function to the sputtering angular emission data of Nelson, Thompson, and Montgomery.[N3] The cosine distribution, centered about the surface normal, was chosen to represent the monotonically decreasing emission with increasing polar angle. Such a distribution would be a result of uniform isotropic scattering from random centers in the target volume. Representation of preferred emission in the [100] direction by a Gaussian was not fruitful since the planar angular resolution of the collectors in this direction exceeds 10°, and the beam entrant hole prevented sputtered particle collection at the point of maximum emission in these particular measurements. (See Fig. 2-3).

The accuracy of the proposed emission representation can be judged by the 14% or less average absolute percent deviation of the 100 data, whose accuracy is of the order of 10%, utilizing only three fitting parameters. In addition, integration of $(1/S)dS/d\Omega$ over the 2π sr above the target should give unity.

$$\frac{4}{S}\int_0^{\pi/2} d\phi \int_0^{\pi/2} d\theta \sin\theta \frac{dS}{d\Omega}(\theta,\phi) = B_{1/2} + 4B_2\sigma^2 = 1. \qquad (2\text{-}2)$$

This condition of conservation of particles is met to within 11% using the values of B_1, B_2, and σ obtained from regression analysis. The integration also provides the relative contributions of the cosine ($B_{1/2}$) and Gaussian ($4B_2\sigma^2$) emissions. The quantities $B_{1/2}$, $4B_2\sigma^2$, $B_{1/2} + 4B_2\sigma^2$, and σ, as well as the measured yield S are shown in Table 2-1.

Three features of the analysis are noted: (a) The Gaussian distribution accounts for 18% or less of the emitted particles, thereby demonstrating the second-order effect of preferred emission at high yield along the close-packed directions. Furthermore, the relative contribution of Gaussian emission decreases with increased ion energy. Obviously, cosine emission is the major sputtering mechanism. (b) There is, again, no significant dependence upon temperature. (c) The angular width of Gaussian emission is comparable to the collector angular resolution, thereby vitiating interpretation of this variable and suggesting improved resolution in future measurements.

These experimental results suggest that in the region of normal incidence and high yield, focused chains, if present, are of secondary importance. It should be noted that the small amount of preferred emission in the close-packed direction could be attributed to two or three (noncolinear) collisions as discussed by Harrison et al.[H1]

2.2.3 Angular Distribution Measured at Non-Normal Incidence

Lack of azimuthal symmetry, inherent at $\alpha = 45°$, precluded convenient nonlinear regression analysis of the angular distribution measurements. Certain qualitative aspects, however, were apparent in the data. The distribution again was characterized by preferred emission along the four <110> directions superimposed upon a background distribution skewed in the direction away from the incident beam. As noted at normal incidence, the preferred emission was of secondary importance.

Further qualitative features are evident in Figs. 2-6 and 2-7, in which the percent collection in each quadrant of the fourfold symmetric collector is plotted as a function of energy. The effect of tilting the ion beam away from normal incidence, evidently, is more important at the lower range of energy than at the higher energy. Under this condition, it can be conjectured that the initial momentum of the ion is dissipated throughout a larger lattice volume with the resultant distribution approaching that for normal incidence. Again, the importance of the depth of the collision below the surface is thought to be a primary factor in the emission of sputtered particles, whereas focused collision transport to the surface is thought to be a secondary consideration.

3. Yield and Angular Distribution of Cesium-Sputtered Molybdenum

3.1 Apparatus and Experimental Procedure

The apparatus described in Section 2 was modified for this series of measurements. Specifically, the alternating potential ion transport system was improved. A long focal length, einzel lens, added immediately upstream from the collector-target assembly, focused and collimated the beam such that 95% of the current was contained in a circular target area 1/4 in. in diameter and in a cone of half-angle less than 4°.

Since the sensitivity of the technique is limited by the radiation hazard of the target, a 0.030-in.-thick disc was spark sliced from a 1/2-in.-diam single crystal and then spark planed to a thickness of 0.020 in. Electropolishing, using concentrated H_2SO_4 at room temperature with 8 to 10 V and 50 mA/cm^2, reduced the target to final size and removed the volume damaged by spark planing. Laue x-ray diffraction showed no indication of damage. The crystal, mounted in an aluminum holder, was further x-rayed to insure alignment of the <100> direction to within 1° of the center of the ion-beam cone. The target and holder were irradiated in a thermal neutron flux of 1.5×10^{13} neutrons cm^{-2} sec^{-1} for 20 h in order to form 66-h half-life ^{99}Mo by neutron activation of 24% abundant ^{98}Mo. During irradiation, the target received 1.6×10^{17} neutrons/cm^2 integrated fast neutron flux. It is unlikely that this caused any significant concentration of lattice defects. Grey[G3] measured a density increase of 0.041% in Mo following fast neutron bombardment of 2.3×10^{19} neutrons/cm^2. Assuming a linear relationship between defect concentration and dose, and using Seitz and Koehler's[S2] contention that the volume increase per vacancy-interstitial pair is equal to twice the

atomic volume, the resultant defect concentration in our target is of the order of parts per million, and therefore negligible compared to the heavy ion-induced damage of the sputtering process.

Following accumulation of 20 mC of integrated cesium ion current, each collector was analyzed by gamma spectroscopy techniques. Absolute determination of the number of sputtered particles on each collector was obtained by comparison with a Mo standard of known weight irradiated with the target.

3.2 Results and Discussion

3.2.1 Yield

The total yield (atoms/ion) is presented in Fig. 3-1 as a function of cesium ion energy ($1 \leq E \leq 7.5$ keV) and target temperature ($77° \leq T \leq 473°K$). The yield rises monotonically with ion energy at all temperatures at which data was taken, but the derivative $(\partial S/\partial E)_T$ at higher energy is decreasing and is indicative of a maximum at energies greater than that reported here. It is assumed that a maximum occurs at higher energies as a result of competition between increased energy transfer per primary collision and decreased probability of a collision in the surfaced layers.[H1] The latter effect is accentuated in the case of bombardment parallel to low index directions[K1] and accounts for the low yield values reported here in comparison to 5-keV Ar^+ sputtering of polycrystalline Mo as reported by Almen and Bruce.[A1] On the other hand, the agreement between our data and that of Carlston et al.[C3] is excellent. In particular, they measure a yield of 1.3 for 5-keV Ar^+ bombardment of (100) Mo at 200°C; whereas, we measure 1.35 for 5-keV Cs^+ bombardment of the same face and at the same temperature. The agreement is considerably better than

expected. It may be that for normal bombardment of a low-index face, the mass of the ion is of secondary importance in comparison to the energy of the ion.

The effect of target temperature on the sputtering yield can be noted by considering the derivative $(\partial S/\partial T)_{E=5\ keV}$ which is negative in the temperature range reported here, but at the higher temperature range ($473°K \leq T \leq 1273°K$) measured by Carlston et al., the derivative is zero for the (100) face and slightly positive for the (110) face. Interpretation of these results is difficult. Carlston et al., suggest that the primary effect of temperature on the sputtering process lies in the thermal dependence of Silsbee[S3] chains. Other experimental and theoretical studies[F1,S4,N3] of the subject have also stressed the importance of focused chains, although from a variety of viewpoints. As an example, thermal annealing of ion-induced defects would lengthen the chains. This implies that $(\partial S/\partial T)_E > 0$ at temperatures where annealing is important and equal to zero at higher temperatures where small deviations from zero can be attributed to second-order effects such as large surface atom thermal vibration.

Harrison, Johnson, and Levy,[H1] and Schlaug and Amster[S8] have recently questioned the importance of chains in the sputtering process and have emphasized the importance of bombardment ion channeling. If this is the case, then the primary effect of thermal annealing is the removal of interstitials residing in the low-index channels. This will reduce the sputtering yield by increasing the probability of ion penetration, i.e. $(\partial S/\partial T)_E < 0$ in the annealing range and equal to zero at higher temperatures.

The annealing range in Mo can be inferred from the fast neutron radiation damage measurements of Kinchin and Thompson[K2] and Grey.[G3] The former concluded that all interstitials created by low-temperature fast-neutron bombardment are annealed when the target temperature is raised to 473°K. In similar measurements, Grey concluded that complete annealing does not occur until the Mo target reaches 1073°K. If the contentions of Kinchin and Thompson are correct, i.e., if annealing is essentially complete at T = 473°K, then our data, in conjunction with the argon-molybdenum data of Carlston et al.,[C3] support the importance of annealing on ion penetration in (100) Mo.

3.2.2 Angular Distribution

It was hoped that the quantitative angular emission data which is easily obtained as a result of the sensitivity of the radioactive tracer technique would offer added insight similar to the work by Anderson et al.[A3] of temperature-dependent Ge sputtering. However, the results are inconclusive.

Preferred emission in the <100> direction, which increased with ion energy but was unaffected by temperature, was evident (see Fig. 3-2), but emission in the close-packed <111> direction could not be discerned. A related measurement of Mo sputtering has been reported by Cunningham and Ng-Yelim[C4] who noted that the <111> emission is less than <100> emission and in some cases is absent. They attribute this to the "(110) content of the surface." On the other hand, Anderson[A2] and Nelson[N4] have detected additional, higher-index spots (preferred emission) in the neighborhood of the <111>. As a result, it is concluded that the angular resolution of the present apparatus must be

improved before definitive measurements of close-packed emission in Mo can be made.

Since the data decreased monotonically with the polar angle θ, the following analytic function was chosen to describe the 100 angular data points:

$$(2\pi/S)(dS/d\Omega) = A \cos^N\theta, \tag{3-1}$$

where A and N are calculated by nonlinear regression analysis to yield the least-squares error between the data and Eq. (3-1). These results, in which the average absolute percent deviation was 10%, are plotted in Fig. 3-3 as functions of temperature and ion energy. The peak parameter N increases monotonically with temperature and with ion energy while the coefficient A can always be equated (within 3%) to N + 1. Use of Eq. (3-1) with the requirement that $\int_{2\pi} d\Omega (dS/d\Omega) = S$ yields the same condition, i.e., A = N + 1. Hence, extrapolation of the angular data measured in the upper plane of the collector to the entire 2π sr above the target is in agreement with the concept of conservation of sputtered particles.

The variation of N with energy and temperature is in qualitative agreement with the contention that ion penetration is a major mechanism in the measurements reported here. If sputtered particles were emitted isotropically from the surface layer, $dS/d\Omega$ would be constant. An amorphous (or heavily damaged) surface with no ion penetration would most nearly approximate this condition in sputtering. As penetration increases either as a result of higher ion energy or annealing of the damaged surface, one would expect emission to become more concentrated at small

values of the polar angle since subsurface layers of atoms become part of the ejection process. Within the angular resolution of our measurements, this seems to be the case. Clearly, improved angular resolution is necessary before more definitive conclusions can be drawn.

4. Cesium Ion Sputtering of Aluminum

4.1 Introduction

A major factor contributing to discrepancies in early sputtering data can be attributed to the interaction of the constituents of the vacuum system with the target surface during sputtering, a process that could conceivably provide a far more active surface than encountered in equilibrium situations. Since the ease of formation and the tenacity of aluminum oxide (Al_2O_3) films formed at the metal surface are well-known,[G4] yield measurements (Al atoms/Cs ion) were made in the presence of an oxygen atmosphere of known partial pressure. This was varied from a clean surface condition, where the flux of oxygen molecules to the surface was an order of magnitude less than the flux of sputtered aluminum particles from the surface[Y1] to a saturation condition, where it is conjectured that sputtering was impeded by a fully developed, alumina film on the target surface. The tenacity of the film and its impedance to sputtering are illustrated by the data.

The yield was determined by a neutron-activation technique. The measurements were made using monocrystalline targets of known orientation since polycrystalline target data obscure some of the essential features of sputtering. Data are presented for normal bombardment of the (110) face of a monocrystalline aluminum target at a temperature of 20°C and for total pressures of 10^{-6} to 10^{-9} Torr. The energy of the cesium ions was varied from 1 to 10 keV.

The short (2.30 min) half-life of ^{28}Al, which is the only radioactive isotope that can be produced by neutron irradiation

of natural aluminum, precluded the use of the radioactive tracer technique developed for the investigation of cesium-copper sputtering. However, neutron activation analysis of the collected sputtered aluminum is possible. Since ^{28}Al quickly approaches saturation activity, very short irradiation periods which conveniently discriminate against most neutron activated contaminants can be used.

The experimental apparatus has been previously described. A cryogenic pump consisting of liquid-nitrogen-cooled, flat copper plates (total active area equal to 1000 cm^3) surrounding three sides of the target-collector assembly was added to condense residual gases and to reduce the pressure. The apparatus is illustrated in Fig. 4-1. The base pressure of the target chamber was 4×10^{-9} Torr while that of the source chamber was 2×10^{-8} Torr without recourse to baking. The pressure differential could be maintained since the two chambers are connected by only the ion beam entrant hole which is 3/8 in. in diameter. During operation of the ion source and while sputtering the aluminum targets, the base pressures increased to 2×10^{-7} Torr in the source chamber, and 2×10^{-8} Torr in the target chamber. In order to observe the effect of an oxygen atmosphere and the assumed presence of Al_2O_3 on the target surface, the target chamber was fitted with a variable leak valve to control the oxygen pressure.

The target and collector assembly are illustrated in Fig. 4-2. The target was spark cut from a single crystal of aluminum. The crystallographic orientation was determined by Laue x-ray back

diffraction techniques, and the crystal was aligned within one degree with the (110) face normal to the ion beam. The collector assembly consisted of a 3.4 in. i.d. stainless steel cylinder 2 in. high which enclosed the target and surrounded the beam hole. The actual collector, which lined the inside of the cylinder, was 0.001-in. lead foil of 99.9999% purity before rolling. Difficulty was encountered in finding a suitable collector, since the foil had to contain less than 1 ppm aluminum, could not contain any impurities that would interfere with the ^{28}Al gamma peak at 1.78 MeV, and could not become even moderately radioactive itself since immediate counting following irradiation was essential. The lead foil was found to meet these requirements and to contain less than 0.5 ppm Al. The foils were always irradiated with an aluminum standard prior to sputtering to establish a background and to verify the suitability of the foil. Following sputtering, the foil was again irradiated with an aluminum standard of known weight. The irradiations were carried out in a pneumatic "rabbit" facility to allow immediate counting following the irradition. Gamma-ray detection and counting were performed in a completely shielded scintillation counter, and the amount of sputtered aluminum was determined by comparison of the ^{28}Al gamma peaks of the foil and the standard. All background varying in a linear manner with energy in those channels associated with the peak in question was eliminated by computing the 1.78-MeV photopeak area by Covell's method.[C5] A second gamma spectrum obtained more than ten ^{28}Al half-lives after irradiation established the foil background contributing to the peak. Corrections for dead time and for the diminishing decay rate during the counting time were applied in the analysis.

4.2 Results and Discussion

4.2.1 Sputtering Yield

The sputtering yield S (atoms/ion) is shown in Fig. 4-3 as a function of the incident ion energy E for the clean surface condition. It should be noted that the target initially had a surface layer of Al_2O_3 resulting from exposure to air. Since ion bombardment occurred at pressures of 10^{-8} Torr, the surface remained clean once this layer was removed by sputtering. The bombardment time was long in comparison to that required for removal of the surface layers. Hence, the initial discrepancy did not contribute significantly to the total yield and therefore did not affect the measurement. The reproducibility of the data was within ten percent, and the general shape of the curve compares favorably with that of the recent S(E) data presented by Daley and Perel[D1] for cesium ion sputtering of polycrystalline aluminum with ion energy variation from 0.5 to 15 keV. Both measurements indicate a saturation in the yield at higher energies, but no evidence of a maximum and subsequent decrease with energy can be detected within the measured energy range. Quantitative agreement exists between the two curves at low energy ($E < 2.5$ keV), but our monocrystalline data does not exhibit as pronounced an increase in yield with increased ion energy. The Daley and Perel data are described as being in good agreement with xenon sputtering of polycrystalline aluminum as reported by Wehner.[W2] Hence, the discrepancy at higher energy can probably be attributed to the nature of targets in the two experiments.

Although a direct comparison of the sputtering of monocrystalline and polycrystalline aluminum targets has not been made, it is interesting to note that significant variations in the sputtering yield of single-crystal copper targets being bombarded with noble gas ions has been reported. Almen and Bruce[A1] noticed a factor of three difference in yield as a result of rotating a single-crystal copper target while bombarding with a 45-keV krypton ion beam. Southern, Willis, and Robinson[S6] reported a factor of two variation in 1-5 keV copper sputtering by argon ions when the angular orientation of the target with the respect to the beam was changed. A variable parameter, first collision model that considered the relative openness of the low-index crystallographic directions compared favorably with these results.

It is believed that a similar situation exists with respect to the monocrystalline and polycrystalline cesium-aluminum sputtering. At low energy ($E < 2$ keV), the appropriate hard sphere diameter of the cesium-aluminum atomic interaction precludes any significant penetration of the ion through the relatively open channels parallel to the close-packed <110> direction. Hence, in this range, the mono- and polycrystalline yields compare favorably. However, as the ion energy increases, the hard sphere diameter (i.e., range of interaction) decreases and penetration becomes favorable for those ions proceeding parallel to a low-index or close-packed direction.[K1] Clearly, greater ion penetration implies less momentum transfer in the surface layers which results in an apparent saturation (and eventually a maximum) in the sputtering yield as the energy of the ion is increased. In the polycrystalline case the high-energy ions are only randomly

aligned with low-index directions so that significant penetration occurs infrequently or at much higher energies. Hence, a continuing increase in yield at high energies can be noted, wheres for monocrystalline sputtering where the ion is moving parallel to low-index directions, the yield reaches a saturation point.

4.2.2 Effect of Oxygen Partial Pressure

The effect of a tenacious surface film on the sputtering yield was examined by creating an oxygen environment of controlled and variable partial pressure. Thus, the oxygen molecular flux to the target surface could be varied. An oxygen poisoning ratio R is defined as the ratio of the rate of arrival of oxygen molecules at the target surface to the rate of removal of sputtered aluminum atoms from the surface. Using the perfect gas concepts of kinetic theory, 11.5 liters sec^{-1} cm^{-2} of O_2 will strike a surface at 20°C.[M2] The poisoning ratio R is then given by

$$R = \frac{6.4 \times 10^7 \ PA}{SI} \tag{4-1}$$

where P is the pressure in Torr, A is the area in cm^2, S is the sputtering yield, and I is the ion current to the target in μA.

The effect of the presence of oxygen is illustrated in Fig. 4-4. The sputtering yield, in aluminum atoms sputtered per incident ion, is plotted vs the oxygen poisoning ratio. The oxygen partial pressure was determined by the change in pressure of the system due to the opening of the oxygen leak valve with account taken of the calculated oxygen partial pressure at base conditions where significant.

The data show, as one would expect, that as the oxygen

poisoning ratio increases, the sputtering yield decreases from that associated with the pure aluminum surface ($R < 0.1$) and approaches a saturation value for $R > 10$. It is assumed that the decrease can be associated with a partial formation of an Al_2O_3 film and that the saturation yield will be close to that of pure alumina.

It is expected that measurements of this type will find application in the prediction or explanation of sputtering effects encountered in space simulation testing of ion rocket engines. Since the vacuum conditions of a space mission can rarely, if ever, be achieved in simulation chambers, the effect of residual gases upon sputtering, especially ion rocket accelerator electrode sputtering, is of importance. It is hoped that the results from experiments of the nature described here may be used for extrapolation of ion engine simulation tests to the results expected in an actual space mission.

5. Cesium Ion Bombardment of Aluminum Oxide in a Controlled Oxygen Environment

5.1 Introduction

Previous work on the cesium ion sputtering of aluminum has shown that surface oxide films strongly affect the sputtering process. Measurements on bulk oxide material have been made and are reported here. In conjunction with the oxide film data, they should contribute to further understanding of this particular aspect of the sputtering process.

The sputtering yield of aluminum oxide was determined by the previously described neutron activation technique in which sputtered aluminum atoms were collected on high purity lead foils and subsequently activated by neutron irradiation. Data are presented for normal bombardment of the (001) face of a monocrystalline aluminum oxide target for ion energy variation from 2.5 to 10.0 keV, temperature variation from 77°K to 425°K, and variation from 0.05 to 10.0 of the ratio of the background molecular oxygen flux arriving at the target surface to the sputtered atom flux (including atom oxygen) leaving the surface.

Other measurements on metallic oxides have been reported by Wehner, et al.[W3] Polycrystalline metal samples with oxidized surfaces and compressed oxide power pellets were used as targets for 3-10 keV H and He ion bombardment. Thin metal films of nickel and silver were evaporated onto the target surfaces to conduct away heat and ion current. The ions spent in eroding the metal coatings were calculated from known sputtering yields and subtracted in computing the oxide yield. It was assumed that charge

migration to the metallic film surrounding the area of the incident ion beam would dissipate charge buildup. The results are not directly comparable to the cesium ion sputtering results since light ions and polycrystalline targets were used. However, reductions by factors of 2-3 in the yields of the metal atoms from the oxides relative to the metals were noted, which is consistent with the results presented below.

Cathode sputtering of mica, fused quartz, and glass by krypton ions has been studied by Akishin et al.[A4] In these experiments, positive charge buildup was neutralized by an electron beam from a thoriated tungsten emitter. Sputtering yields were calculated from loss of target weight.

Other techniques of dielectric sputtering in noble gas plasmas using rf fields at the target to neutralize charge buildup with plasma electrons have been suggested.[A5,J1] However, none of these results are suitable for comparison with the present data.

5.2 Experimental Technique

The experimental apparatus has been described above; however, the dielectric properties of aluminum oxide required neutralization of positive charge accumulation on the target surface and external monitoring of the ion beam current. Surface neutralization was accomplished by inserting an electron emission filament (0.02-inch-diameter tantalum wire) on one side of the ion beam between the target and the collecting foil holder (Figure 5-1). Resistance heating of the filament produced a compensating electron emission current at the target surface. Calibration, using a metallic

target from which the electron current could be monitored, showed that a positive bias of 30 volts on the target produced an electron current of 35 uA to the target surface. Since the maximum ion current to the target was less than 30 uA, target self biasing as a result of charge accumulation could not exceed 30 volts - a negligible amount in comparison with the ion accelerating voltage. Negative charge accumulation under these conditions is not a problem.

To measure the ion beam current, a small hollow cylinder capped at the top and bottom was attached to, but insulated from, the collector plate. The cylinder was 3.4 inch in height and one inch in diameter with a 1/8-inch-diameter hole in the top plate and a 1/2-inch-diameter hole in the bottom plate. The cylinder, which hung from the collector plate into the collimating tube, served as a Faraday cup when biased at a positive potential of 35 v. This bias provided a final focus and collimation of the beam but, more importantly, ensured correct measurement of the ion beam current since it suppressed the loss of secondary electrons from the cup. A higher positive potential was applied to the collector plate assembly (45 v) since electrons from both the tantalum emitter and the target could reach the Faraday cup.

The current was measured by applying a high voltage through an auxilliary circuit to one set of deflector plates in the collimating tube, thus deflecting the ion beam into the side of the cup. Upon removal of the over-ride voltage, the beam returned to its normal course through the center hole in the top of the cup and onto the target. Since the entire beam did not pass through the center hole, a current reading from the cup existed at all times, and the current

delivered to the target was the difference between the deflected and undeflected currents. As a result of steady source operation, current monitoring every three minutes was sufficient. Electrons from the tantalum wire did not present a problem since their emission was independent of ion beam current. However, secondary electrons striking the cup are produced only when the beam is on the target and would therefore be a function of the ion beam current. To ensure elimination of this effect, a small horse-shoe magnet was impressed into the target holder, creating a surface field of 100 gauss. This was sufficient to deflect the secondary electrons leaving the target into the collector assembly but had negligible effect on the ion beam. A check on the operation of the entire system with a metallic target verified the accuracy of the current measurements and showed that the ion beam did not strike any part of the collector assembly after passing through the Faraday cup.

5.3 Results and Discussion

5.3.1 Effect of Ion Energy

The cesium ion energy dependence of the sputtering yield of single crystal aluminum oxide in the 2.5-10.0 keV range is illustrated in Figure 5-2. In the kilovolt ion energy region the yield increases gradually with increasing ion energy. At lower ion energies, the yield would be expected to rise sharply with increasing energy from the zero point with a rapidly declining rate of increase. This behavior is common to yield versus energy relationships in sputtering and results from competition between increased energy transfer per collision and decreased probability of collision near the surface (channeling[K1]) as the energy of the ion is increased. Since the <001> direction in the hcp, Al_2O_3 crystal does

not afford a high degree of openness, a continuing increase in yield rather than a maximum for $2.5 < E < 10$ keV seems reasonable.

5.3.2 Effect of Oxygen Partial Pressure

A series of yield measurements for normal bombardment of Al_2O_3 at 60°C by 10 keV cesium ions was made in which the oxygen background partial pressure was varied. The results are shown in Figure 5-3 as aluminum atoms sputtered versus the poisoning ratio, R, which has been previously defined as the ratio of the rate of arrival of residual oxygen molecules at the target surface (calculated by a perfect gas model) to the rate of departure of the sputtered atoms (including oxygen atoms). The yield exhibits little change over the designated range of poisoning ratio. The slight negative slope in the neighborhood of $R = 1$ can be related to the interatomic binding of the surface atoms. When an oxygen atom is sputtered under the condition $R \ll 1$, the neighboring aluminum atoms are less tightly bound and therefore more easily sputtered. For $R \gg 1$, the sputtered oxygen atom is replaced from the residual environment before a neighboring aluminum atom can be sputtered from the more weakly bound state.

A direct comparison between the effect of oxygen partial pressure on aluminum and on aluminum oxide is made in Figure 5-4. As expected, the aluminum yield is strongly influenced by the formation of surface oxides; whereas, the Al_2O_3 is already in its most oxidized state and therefore oxidation is not as influential a factor. It is interesting to note that the yield from aluminum at $R \gg 1$ is essentially the same as that from aluminum oxide at $R \ll 1$; thus supporting the contention that in the case of aluminum, a surface oxide film is maintained at high pressures.

The decrease in both yield curves near a poisoning ratio of unity suggest that further investigation of the events occurring at the target surface in this region might prove fruitful.

5.3.3 Effect of Temperature

The sputtering yield of Al_2O_3 decreased with increasing temperature as shown in Figure 5-5. Auxiliary measurements on monocrystalline aluminum indicated little temperature dependence in the sputtering yield, as do the results reported above for copper. For molybdenum however, a decrease in the yield with increasing temperature has been found. (See section 3.) Similar results have been obtained in other measurements[C3,A3] and are usually attributed to annealing of lattice defects produced by ion bombardment. The present results further indicate that the temperature dependence stems from changes in the rate of annealing of the lattice defects produced near the surface by ion bombardment. It is assumed that these defects impair ion penetration into the lattice, resulting in expenditure of more energy of the incident ion near the surface and, hence, increasing the sputtering yield. Since the annealing rate increases with temperature, the removal of defects increases, ion penetration increases, and the sputtering yield decreases. For the relatively low melting aluminum (932°K) and copper (1356°K), the annealing occurs rapidly enough at low temperature to preclude any temperature effect, but for the higher melting molybdenum (2890°K) and aluminum oxide (2310°K), the annealing rate changes significantly between 77°k and 475°K. At high temperatures (beyond the present range of our apparatus), where annealing is rapid enough to be insensitive to temperature change, one would expect lattice vibrations to become significant, and further decrease the yield.[N2]

6. Determination of Angular Distribution of Cesium Ion Sputtered Aluminum Atoms by Electron Microprobe Analysis

6.1 Introduction

In the angular distribution measurements of cesium ion sputtering reported above, a radioactive tracer technique was incorporated which is suitable when long-lived isotopes are considered but is unsatisfactory for aluminum which has a 2.3 minute half-life. Since numerous post-sputtering irradiations of collectors is unfeasible, a technique was developed in which the sputtered aluminum atoms were collected on highly polished copper collectors and then scanned by an electron microprobe[M4] to determine the variation in the relative surface density of aluminum.

The electron microprobe is a sophisticated tool for the chemical analysis of minute volumes. Electron beam bombardment excites characteristic x-rays from target elements which are then monitored by an in-vacuum detection system. Since no depth corrections are required, thin film (single or multi-component) analysis is especially suitable for the microprobe.

Measurement of optical density has been a popular method for the determination of thin (sputtered) film thickness.[N2,R1,Y2] The photodensitometer technique can provide absolute data more easily than the microprobe, but low sputtering yields and low ion beam currents require long sputtering periods to produce films for optical density measurements. The ability to analyze multi-component films and unevenly oxidized films strongly supports the choice of the microprobe for these measurements.

Sputtering runs were made at cesium ion energies from 5.0 to 10.0 keV and at temperatures from 77°K to 475°K. In all cases the cesium ion beam was normal to the (100) face of the monocrystalline aluminum target, and the angular distribution of the sputtered atoms was determined in the (001) plane. The raw data were correlated to give the relative sputtering yield per unit solid anlge versus polar angle.

6.2 Experimental Technique

The target and collector assemblies are shown in Fig. 6-1. The copper collector cubes were highly polished to ensure uniform intensity of the electron beam across the face of each collector. Before use in a sputtering run, each cube was placed in the microprobe and counted to ensure that x-rays occurring in the aluminum K_α wavelength region were less than 10% of the expected yield following collection of sputtered aluminum.

The cubes were aligned along the collector plate in the desired crystallographic plane relative to the target. After 60-70 microcoulombs of ions had been delivered to the target, the cubes were removed and placed in the microprobe, which held a maximum of four samples. The 7 keV electron beam delivered 0.05 micro-amperes to a 25 micron diameter target area. The value of 7 keV was chosen to prevent excitation of K_α x-rays of copper (8.05 keV) and the subsequent secondary excitation at 1.56 keV of the K_α x-rays of aluminum. Each cube was scanned at 1,000-micron intervals, representing a one-degree interval at low polar angles and about one-half degree at high angles. The raw data were corrected for background and the relative distribution curves from each collector cube were combined to

give the total angular distribution. The data were joined smoothly at the junction points of the cubes, but the measured relative distributions were maintained. This guarded against false discontinuities in the total curve arising from a slightly different surface condition on the collector cubes and/or variation of the counting efficiency in the microprobe, which can occur when samples are changed.

6.3 Results and Discussion

The angluar distributions of sputtered aluminum atoms from the (100) face of a monocrystalline target at cesium ion energies of 5.0, 7.5, and 10.0 keV are shown in Fig. 6-2. The curves are normalized to unity at a polar angle of 6° and indicate that the relative distribution at higher angles decreases with increasing ion energy. With increasing energy, the ions penetrate more deeply into the crystal and forward scattering (i.e., low polar angle) is enhanced. Thus, the relative amounts sputtered at higher angles decrease.

Similar peaking at 27° and 45° is noted in all of the curves. The peak at 45° has been observed in many reports of sputtering of fcc crystals. While this peak has normally been attributed to focused collisions along the close-packed <110> direction, no such chain exists at a 27° polar angle. The occurrence of this peak supports the premise that preferred sputtering directions are a function of the regularity of the lattice and that focusing along close-packed directions, if present, is a secondary effect.

The effect of temperature on the angular distribution is illustrated in Fig. 6-3. Curves for sputtering at 77°K, 298°K, and 475°K with a 7.5 keV cesium ion beam are shown. No significant

temperature dependence is evident, as previously noted for copper. The lack of a temperature effect is attributed to rapid annealing in both metals in the designated temperature range.

6.4 Conclusions

The technique as developed provides an additional method for investigating the sputtering process and thin surface films. The accuracy attained from the high resolution of the microprobe is degraded, however, by ion beam focus limitations, surface conditions of collectors, fluctuations in the detector system, and possible atom migration on the collector surfaces. The present results were reproducible within 10-20%. The technique is tedious as a result of limited capacity and versatility of commercially available electron microprobes. However, improvement in both categories is a matter only of design and not of technology. In addition, a straight line traverse capability covering at least one inch would be a major improvement for sputtered film investigation.

7. Mercury Ion Sputtering of Cu, Mo, and Ni

7.1 Introduction

The experimental method for study of mercury ion bombardment of copper, molybdenum, and nickel was similar to that described in Section 2, cesium ion sputtering. The RTT, in conjunction with a mosaic collector, was used to measure yield and angular distributions of sputtered copper and molybdenum. Because of its short half-life, only the total yield of nickel was measured. The new collector assembly offered improved angular resolution and, thereby, gave more detail to the sputtering distribution. The results are tabulated and have been fit with similar analytic functions.

7.2 Experimental Technique

A schematic illustration of the experimental apparatus is presented in Figure 7-1. The primary components were electron bombardment ion source, electrostatic ion beam transport system, magnetic analyzer, and target-collector assembly. As illustrated, these components were mounted in their respective vacuum chambers which were differentially pumped so that sputtering occured under clean surface conditions. Typically, the source chamber, which was pumped by a cryogenically baffled, 6" oil diffusion pump, was maintained at a pressure of 3×10^{-7} torr with the ion source in operation. Cryogenic surfaces in the magnetic deflector chamber provided differential pumping between the source and target chambers, while the latter, which was pumped by a 200 liter/sec ion pump and by a liquid nitrogen cooled cryogenic surface, operated at a pressure less than 5×10^{-8} torr.

Space charge divergence of the ion beam was compensated by an electrostatic transport lens system, consisting of a series of einzel lenses. The ion beam was accelerated from the source to an energy of 7.5 keV and transported at this energy by the lens system through the magnet chamber to the target where the desired beam energy was selected by appropriate biasing of the target, as shown in Figure 7-2. The transport system provided a target current density of 10μa/cm^2 over a beam area of 0.40 cm^2. The sputtering rate was significantly greater (typically by a factor of 10) than the rate of arrival of all background gases.

The sputtering angular distribution was measured with a cylindrical mosaic collector which covered only one quadrant. (See Figures 7-3 and 7-4.) The angular resolution was, thereby, increased by a factor of four with no loss of information since the target crystal orientation provided four-fold symmetry. The remaining sectors of the solid angle above the target were fabricated from aluminum foil.

7.3 Results and Discussion

7.3.1 Yield

7.3.1.1 Normal Incidence

Total yield values (± 6%) obtained for normally incident Hg^+ ions on (100) surfaces of copper, molybdenum, and nickel single crystals are displayed in Figure 7-5, as a function of ion energy. For all targets, the yield is a linear function of energy between 1 keV and 5 keV; a broad maximum occurs near 7.5 keV.

7.3.1.2 Oblique Incidence

For 7.5-keV Hg^+-ions, the total yield from a Cu (100) surface was measured for angles of incidence α = 0°, 18°, 45°, and 63° (corresponding to the <100> , <43, 10, 10>, <755>, and <7, 10, 10> directions) from the target-surface normal (see Figure 7-6). A more structured relationship than that shown is anticipated as a result of channeling along low index directions. However, considably more data, similar to that of Molchanov, et al.,[M3] is required.

7.3.1.3 Temperature Effects

At 7.5 keV, the molybdenum yield at 480°K was within 2% of the yield at 300°K. This result is consistent with that of Carlston, et al.,[C3] who noted that the yield from a Mo (100) surface under 5 keV Ar^+ bombardment was independent of temperature for $350 \leq T \leq 1000$°K.

7.3.2 Angular Distribution

7.3.2.1 Normal Incidence

Preferred emission from the Cu (100) surface was noted in the <110>, <112>, and <100> directions. The <110> peak was the most intense, while the <112> peak was weaker with greatest intensity at an ion energy of 1.0 keV. These results are similar to those observed by Nelson and Thompson[N1] for 10-keV A^+-ion bombardment of Cu (100).

Preferred emission from the Mo (100) was noted in the <111>, <110>, and <100> directions. The <110> peak was always weak. The most intense peak at lower energies was the <111> peak, but at higher energies the <100> peak dominated. The angular resolution was not sufficient to resolve multiple peaks (if present) near the

<111> direction as reported by Anderson[A3] and Nelson,[N4] and near the <110> direction as reported by Anderson.[A3]

A more accurate analytic expression was chosen to represent the angular emission data.

$$\frac{2\pi}{S}\ \frac{dS(\theta,\Phi)}{d\ \Omega} = B_1 \cos\ \theta + B_2 \exp\left[-\frac{\psi^2\ (\theta,\ \Phi;\ B_4,\ B_5)}{2B_3{}^2}\right] + B_6 \exp - \left[\frac{\theta^2}{2B_3{}^2}\right] \tag{7-1}$$

where

$$(\theta,\Phi;B_4,B_5) = \cos^{-1}\ [\cos B_4\ \cos\ \theta + \sin B_4\ \sin\ \theta\ \cos\ (B_5 - \Phi)]$$

It was assumed that all Gaussians had the same mean angular width. Although this assumption was consistent with previous measurements, validation was made with one set of data for 10-keV Hg^+-ion bombardment of molybdenum. The check revealed that the variation of the mean-width was less than five percent.

Fitting Eq. (7-1) by non-linear regression analysis to the angular distribution data provided the parameters listed in Tables 7-1 and 7-2 for the copper and molybdenum normal incidence data. Integration of $\frac{2\pi}{S}\frac{dS}{d\Omega}(\theta,\Phi)$ over the solid angle subtending the target defined the relative contributions to the total sputtering yield of the randomized lattice effect and the two directional effects. It should be noted that integration of the Gaussian terms over the solid angle is dependent only on the amplitude and mean-width of the Gaussian and is independent of the angular position. Hence, the values of the second and third

terms must have the same form, although the second term contains an additional factor of four because the entire close packed direction, <cpd> , Gaussian lies within the limits of integration, whereas only 1/4 of the <100> Gaussian is within these limits. With the expansion

$$\sin \theta \simeq \theta - \frac{\theta^3}{3!} \quad \text{for} \quad 0 < \theta < 1 \tag{7-2}$$

the integral of the third term, I_3, of Eq. (7-1) becomes

$$I_3 = \frac{\pi}{2} B_6 \left\{ B_3^2 \left[1 - \exp\left\{ - 1/2 \left(\frac{\pi/2}{B_3} \right)^2 \right\} \right] + 0 \left(\frac{B_3}{3} \right)^4 \right\} \tag{7-3}$$

Since $B_3 < \pi/6$, a good approximation to Eq. (7-3) is

$$I_3 = \frac{\pi}{2} B_6 B_3^2 \tag{7-4}$$

Thus, integration of Eq. (7-1) yields

$$1 = \frac{B_1}{2} + 4 B_2 B_3^2 + B_6 B_3^2 \tag{7-5}$$

Eq. (7-5) provides the relative contribution of random lattice emission, $B_1/2$, preferential emission in the <cpd> directions, $4\ B_2\ B_3^2$, or <100> emission, $B_6\ B_3^2$. Figures 7-7 and 7-8 present these contributions as functions of ion energy for copper and for molybdenum. It can be noted that the results for both elements exhibit the same energy dependence. Both have cosine contributions that possess a wide plateau at 5.0 to 7.5 keV and which account for 67 to 91 percent of the sputtered particles. The contributions

for the four <cpd> Gaussians decreased monotonically as the ion energy increased, although above 5.0 keV in copper and 7.5 keV in molybdenum these contributions were essentially independent of energy. Above 7.5 keV, the variance of the <cpd> Gaussians decreased. The greater reduction in the Mo <111> Gaussians, as opposed to the Cu <110> Gaussian, is assumed to be symptomatic of a lower annealing rate and of a higher concentration of mercury atoms in the surface layers of the molybdenum target. The <100> Gaussian contribution increased monotonically with the ion energy for both elements. A similar energy dependence has been observed by other investigators.[Y3, K3, A6, Y4, A7]

Harrison, et al.,[H1] have shown that preferential ejections can be obtained by considering ion-atom and atom-atom collisions in only the first four atomic layers of a perfect lattice. As the ion passes through these layers it has some probability of initiating a sequence of collisions that ultimately results in ejections along directions that depend upon the lattice structure. However, they were not able to assess the relative importance of these surface interactions; thereby obscuring direct comparison with our regression analyzed, experimental data.

7.3.2.2 Oblique Incidence

In the case of oblique-incidence bombardment of Cu (100), the peaks observed were at $\theta \cong 45°$, $\Phi \cong 45°$, and 135°; $\theta \cong 34°$, $\Phi \cong 0°$, 90°, and 180°; and $\theta \cong 0°$. The first pair of peaks were the "back" and "forward" <110> peaks, respectively, and were present for all angles of incidence investigated. Three

<112> peaks were evident at an angle of incidence α of 18°, but as α increased, the "back" and "forward" <112> peaks became hidden in the high background distribution; however, the <112> at $\Phi \cong 90°$ was detectable even at $\alpha = 63°$. The intensity of the <100> peak ($\theta \cong 0°$) changed only slightly with α. The high background distribution became more biased in the forward direction as α was increased from 18° to 63°.

The form of the background (or non-preferential) distribution for oblique incidence is difficult. As in the normal incidence case, this background may be assumed to arise from the randomization of the single-crystal structure. The oblique-incidence results of Stein and Hurlbut[S8] for Xe^+-ion bombardment of polycrystalline potassium targets indicate that at higher energies there is enhanced symmetry in the polar angular distribution and that their high energy distribution (E = .44 keV) approached that given by a cosine. Asymmetry in the background distribution for oblique-incidence A^+-ion sputtering of Cu (100) was also observed by Molchanov, et al.[M3] for 27-keV ions and by Nelson and Thompson[N1] for 10-keV ions. The highest intensity was found in the solid angle opposite to the beam, i.e., in the forward direction.

A simple background distribution for oblique-incidence, which accounts for asymmetry in the forward direction and approaches a cosine distribution at smaller angles of incidence, is a cosine distribution, tilted away from the target normal through an angle β in the forward direction. Since this direction is determined by the projection of the ion beam momentum on to the plane of the target, the tilt angle β is measured in the plane defined by

the target normal and the ion-beam vector.

At oblique incidence, only two-fold rather than four-fold symmetry is present, and therefore, the angular distribution was measured over half of the solid angle subtending the target. Hence, the analytical model assumed Gaussians for the "forward" and "backward" <110> peaks and for the <100> peak with a tilted cosine providing the background distribution.

Thus, the analytic expression chosen to fit the data is

$$\frac{2\pi}{S}\frac{dS}{d\Omega}(\theta,\Phi) = B_1 \cos \psi_t (\theta,\Phi;\, B_2) + B_3 \exp\left[-\frac{\psi_b^2 (\theta,\Phi;\, B_5,B_6)}{2\, B_4^2}\right] + B_7 \exp\left[-\frac{\psi_f^2 (\theta,\Phi;\, B_8,B_9)}{2\, B_4^2}\right] + B_{10} \exp\left[-\frac{\theta^2}{2\, B_4^2}\right] \quad (7\text{-}7)$$

where the fitting parameters are

B_1	=	Amplitude of the tilted cosine distribution
B_2	=	Tilt angle for the tilted cosine distribution
B_3	=	Amplitude of the back <110> Gaussian
B_4	=	Mean-width of all three Gaussians
B_5, B_6	=	Polar and azimuthal angular positions of the back <110> Gaussian
B_7	=	Amplitude of the forward <110> Gaussian
B_8, B_9	=	Polar and azimuthal angular positions of the forward <110> Gaussian
B_{10}	=	Amplitude of the <100> Gaussian

$$\psi_t \quad (\theta,\Phi;B_2) = \cos^{-1} \quad [\cos B_2 \cos\theta - \sin B_2 \sin\theta \cos\Phi]$$

$$\psi_b \quad (\theta,\Phi;B_5,B_6)$$

$$= \cos^{-1} \quad [\cos B_5 \cos\theta + \sin B_5 \sin\theta \cos \quad (B_6 - \Phi)]$$

$$\psi_f \quad (\theta,\Phi;B_8B_9)$$

$$= \cos^{-1} \quad [\cos B_8 \cos\theta + \sin B_8 \sin\theta \cos (B_9 - \Phi)]$$

The "conservation of particles" condition for each set of oblique-incidence data is

$$1 = \frac{B_1}{2} \cos B_2 + 2\, B_3B_4^{\,2} + 2\, B_7B_4^{\,2} + B_{10}B_4^{\,2} \tag{7-7}$$

The relative contributions are: tilted cosine, $(B_1 \cos B_2)/2$; two back <110> Gaussians $2\, B_3B_4^{\,2}$; two forward <110> Gaussians, $2\, B_7B_4^{\,2}$; and <100> Gaussian, $B_{10}B_4^{\,2}$. Figure 7-9 presents the contribution of each of the above for each angle of incidence.

The fitting process revealed that β increased from 7.0° to 11.5° as α was increased from 18° to 63°. This, coupled with the fact that the relative cosine contribution was only weakly dependent on α, is indicative of the deep penetration of the 7.5-keV ions. The surface projection of the momentum of such an ion appears to be isotropically absorbed as a result of the large number of atomic collisions required to transfer momentum to an atom near the surface, which is ejected in a direction essentially independent of the initial momentum. Conversely, atoms

ejected as a result of ion-atom collisions near the surface may be expected to leave the target in a direction dependent upon the input momentum. Thus, the surface interactions described by Harrison, et al.[H1], should be dependent upon the angle of incidence α, and the angular positions of the related preferential-ejection directions should also depend on α. Since the positions of the Cu <110> Gaussians were not influenced by α for the measurements reported here, these surface interaction contributions must be of secondary importance for an ion with a mean range greater than that of a 7.5-keV Hg^+-ion.

8. Measurement of Thin Oxide Films by Characteristic Oxygen K-Shell X-ray Production

8.1 Introduction

The objective of this work was the construction of experimental apparatus capable of on-line measurement of oxygen surface density in the microgram/cm^2 range by the observation of oxygen-K x-rays produced by 100-keV protons. The objective was motivated by almost universal hindrance to surface physics studies by oxide contamination.[H2] Such on-line measurement of oxygen surface densities provides a means of investigating oxide build-up as a function of experimental conditions, e.g., target temperature and oxygen partial pressure. In addition the attainment of clean surface conditions, which is of great importance to many measurements of surface properties, such as the work function and the arrangement of surface atoms (low-energy electron diffraction studies), can be readily determined.

The measurement of surface density by the observation of proton-produced characteristic x-rays was first proposed by Khan, Potter, and Worley[K4] and is based on the direct correlation of the characteristic x-ray yield with the number of surface atoms. In comparison with the usual techniques for surface density measurements,[B1] characteristic x-ray production provides continual measurement of oxygen surface densities even in the presence of other surface contaminants. As opposed to electrons, protons are chosen as the projectiles primarily because of the lack of continuous bremsstrahlung radiation associated with the slowing-down process.[M6] This allows the use of a moderately dispersive detector, without the necessity of employing a diffracting element in the system.

The interaction of an energetic proton with matter involves many inelastic collisions between the proton and the atomic electrons of the medium. At proton energies in excess of one MeV, the stopping power decreases with increasing proton energy. At lower proton energies, i.e., at proton velocities comparable to those of outer atomic electrons, part-time neutralization of the proton by capture and loss of orbital electrons begins to dominate the interaction process, causing the stopping power to peak at approximately 100-keV proton energy. However, in this proton energy range where the maximum energy per unit length is transferred to the target, the complications produced by electron capture and loss have prevented an adequate theoretical description of the interaction process.[N5] Furthermore, only meager stopping power data is available for this energy range.[A8] The lack of important experimental information is largely due to the difficulty of obtaining sufficiently thin self-supporting targets for transmission stopping power measurement. Hence, one of the purposes of the present work was the development of a technique for stopping power measurements in the low-energy proton range (less than 100 keV) which does not depend on self-supporting targets. The stopping power for 20- to 100-keV protons in aluminum oxide was measured by the observation of proton-produced characteristic oxygen K-shell x-rays. The aluminum oxide targets were not self-supporting but were chemically bound to aluminum substrates.

If the inelastic collisions between a proton and the atomic electrons of the target lead to ejection of an inner shell electron, the subsequent filling of the vacancy produces an x-ray

characteristic of the target atom.[M6] The fundamental physical quantity governing the production of characteristic x-rays by protons is the charactistic x-ray production cross section for the target atom electron shell considered. This quantity is important to the understanding of proton interactions with matter, since it is directly related to the ionization cross section through the fluorescence yield.

Since few absolute measurements of the cross sections for K-shell x-ray production have been measured, an additional goal of the present work was the measurement of the K-shell x-ray production cross section for oxygen in the low-energy proton range. The quantity was calculated from the measured oxygen-K x-ray yields (x-rays/proton) from thin targets (target thickness much less than the proton range) of aluminum oxide.

8.2 Experimental Apparatus and Methods

The experimental apparatus, illustrated in Figure 8-1, consisted of: (1) an ion source capable of producing 100-keV protons, (2) a beam analyzing magnet, coupled with two combination cryogenic and titanium sublimation pumps, (3) an ultra-high vacuum target chamber, and (4) a gas proportional counter for characteristic x-ray detection.

8.2.1 Vacuum Considerations

Previous investigators[K5] have observed carbonaceous film build-up on proton-bombarded targets. Such a film would obscure the measurements performed in this study due to overlap of the characteristic carbon K-shell x-ray peak (277 ev) with the characteristic oxygen K-shell x-ray peak (525 ev) in the

gas proportional counter detection system.

Consequently, the hydrocarbon partial pressure in the target chamber was reduced to a negligible value by maintaining an ultra-high vacuum in the target chamber. The target chamber was constructed of stainless steel and pumped by a 400-liter/sec ion pump. All vacuum seals were made using metal gaskets of either copper or aluminum foil. Following a light bake-out at an internal temperature of 175° C for 12 hours, the base pressure of the target chamber was 2.5×10^{-10} Torr, as indicated by a nude ion gauge. The ion source chamber was evacuated using a 1500-liter/sec, cryogenically trapped, oil diffusion pump. The base pressure of the ion source chamber was 1×10^{-7} Torr, increasing to 5×10^{-7} Torr with ion source operation.

To reduce the flow of hydrocarbon molecules from the ion source chamber into the target chamber, two combination cryogenic and titanium sublimation pumps were installed, as shown in Figure 8-1. These pumps were each constructed of 6-inch-diameter by 6-inch-length stainless steel cylinders. Inner copper cylinders having internal areas of 1300 cm^2 were cooled by liquid nitrogen. Commercial titanium filaments were included for periodic titanium sublimation onto the inner copper surfaces.

With one-microamp proton bombardment of an aluminum oxide target, the target chamber pressure increased to 1×10^{-9} Torr. Partial pressure analysis indicated that the hydrocarbon content was less than 5%. The major gas constituents were H_2 (35%), A (30%), H_2O (15%), and N_2 (15%). The target chamber pressure varied directly with the target current. The usual target current

was less than five microamps, corresponding to a target chamber pressure of less than 5×10^{-9} Torr.

8.2.2 Ion Source and Beam Analysis

The commercial* ion source, illustrated in Figure 8-2, is known as a duoplasmatron.[M7] It consists of a three-electrode discharge chamber, extractor electrode, Einzel lens focusing element, and a 100-KV accelerating column. The cathode is a platinum-rhodium mesh, coated with a barium-strontium oxide electron emission mixture.**

The basic discharge is established by introducing hydrogen gas into the discharge chamber and then accelerating thermally excited electrons from the cathode toward the intermediate electrode. The ionization of the hydrogen gas molecules produces a plasma that is concentrated near the aperature of the conically shaped intermediate electrode.

To the basic discharge is added a further electron-accelerating electric field and a magnetic mirror field between the intermediate electrode and the anode. The plasma is thus further concentrated, with almost total ionization of the hydrogen gas, near the 0.008-inch anode aperature.

Ions leaking through the anode aperature are accelerated by an electric field between the anode and extractor and focused by an Einzel lens arrangement. Up to 100-keV final ion beam energy is then established by a 10-element, 100-KV accelerating column.

---

*Radiation Dynamics, Inc., Long Island, New York.

**RAC-336-118

Magnetic analysis of the ion beam indicated the following major components: (1) H_1^+ (25%), (2) H_2^+ (60%), and (3) H_3^+ (15%). The analyzing magnet permitted only the proton component to enter the target chamber. Typically, the target current was five microamps over a 0.3-cm^2 area.

The ion beam energy was measured utilizing a voltage divider, constructed of a series arrangement of ten 500-megohm high-voltage resistors and a 500-K ohm precision resistor. To insure negligible leakage current, the resistor string was suspended in transformer oil within a cylindrical polystyrene case. The voltage divider was calibrated to less than 0.25% maximum error up to 100-KV applied voltage, by calibration of each high-voltage resistor up to 10-KV applied voltage.

The energy spread of the proton beam was investigated by measuring the oxygen-K x-ray yield from a thick target of aluminum oxide, as the beam was swept across the target with the analyzing magnet. At 100-keV proton energy, the yield was constant with a standard deviation of 1%. This standard deviation is completely ascribable to statistical variations in the x-ray count rate and integrated target current measurements. Consequently, the energy spread in the proton beam was negligible. This result agrees with the measurements of von Ardenne, who found less than a ten-ev energy spread from ion sources of this type.[VI]

8.2.3 Target Current Measurements

As shown in Figure 8-3, the proton beam was collimated by a double-disk collimator, the first having a 3/16-inch-diameter aperture and the second a 1/4-inch-diameter aperture. The

collimator assembly was biased +300 v relative to ground to suppress secondary electrons.

The protons then passed through a beam alignment tube with a 1/4-inch-diameter, knife edge exit aperture before striking the target. The beam alignment tube served the dual purpose of limiting the maximum beam divergence to $\pm$ 1.5° and preventing scattered protons or energetic secondary electrons from the collimator from reaching the electron shield or target holder, thereby, producing an erroneous target current indication. Less than 10% of the target current was collected on the alignment tube. To verify that secondary electrons produced at the exit aperture did not interfere with target current measurements, the alignment tube bias was varied from -100 v to +100 v relative to ground with no effect on the target current. Consequently, it was normally maintained at ground potential.

To insure complete collection of charge, a Faraday cage arrangement was used. The electron shield was biased -300 v relative to the target to prevent secondary electrons from leaving the target area. The integrated proton current was measured by a current integrator* calibrated to 1%.

Efficient vacuum pumping in the immediate region of the target was permitted by two, thirteen-cm^2 area holes cut in the top of the electron shield. However, electric field integrity was maintained by covering the holes with 250 lines/inch, 70% transmission nickel mesh. A 3/4-inch-diameter hole was provided for x-ray transmission to the proportional counter.

---

*Model CI-110, Eldorado Electronics, Concord, California.

The target holder was a ten-sided copper heat sink, mounted on a rotatable feedthrough, so that ten targets could be accomodated, but individually rotated into the proton beam. The target normal was oriented 45° with respect to both the proton beam and the direction of x-ray detection. An alumel-chromel thermocouple attached to the target holder indicated less than 2° C temperature rise during target bombardment. According to temperature calculations, the target surface temperature was less than 1° C greater than the target holder temperature.

8.2.4 Characteristic X-ray Detection

The characteristic x-rays produced at the target were detected by a conventional gas-flow (50 cc/min.) proportional counter, as shown in Figure 8-4. The proportional counter was a stainless steel cylinder, 2 inches in diameter by 12 inches in length, with a 0.003-inch stainless steel center wire.

To provide a bakeable ultra-high vacuum target chamber seal with minimal absorption of the low-energy characteristic oxygen K-shell x-rays (525 ev) that were produced by proton bombardment of aluminum oxide targets, a 0.0015-inch aluminum foil gasket with a 1/2-inch-diameter, 1250-Å alumina window was used, as indicated in Figure 8-5. The combination window-gasket assembly was prepared following a procedure similar to that given by Harris.[H3] Both surfaces of the aluminum foil were anodized at 90 v for 10 minutes in an aqueous solution of 3% ammonium citrate. Eight-normal sodium hydroxide was applied to the center area of one surface of the anodized foil, dissolving the aluminum oxide on that area and exposing the underlying aluminum. The foil was then immersed in eight-normal

hydrochloric acid, which dissolved the exposed aluminum, but did not attack the alumina. The final result was a thin alumina window in the center of an anodized aluminum foil.

In order to limit gas diffusion through the thin alumina window, a diffusion-pumped, high-vacuum chamber was located beyond the target chamber window, as indicated by Figure 8-4. This chamber also had a thin, alumina x-ray exit window and was followed by a fore-pumped chamber with vacuum feedthroughs for insertion of absorber foils with the x-ray beam.

The proportional counter window for characteristic oxygen K-shell x-ray transmission was a 5/16-inch diameter, 4000-Å alumina window. It was prepared from an aluminum disk, whose center area was machined to a 0.01-inch thickness.[H4] The disk was anodized and chemically treated following the same procedure used for preparation of the window-gasket assemblies shown in Figure 8-5. The anodization voltage was 290 volts. Backing for the window consisted of 100 lines/inch, 82% transmission nickel mesh, held in place by a 200-gram brass weight. The brass weight also served as an x-ray collimator, having a 1/4-inch diameter aperture. To minimize electric field distortion between the dielectric window and the proportional counter center wire, an additional nickel mesh was placed over the 1/2-inch diameter proportional counter aperture.

Initial x-ray detection indicated a large background count rate due to scattered protons from the target traversing the thin alumina windows and entering the proportional counter. The scattered protons were completely stopped before entering the

proportional counter by the insertion of an additional alumina window (290-v anodization voltage) into the x-ray beam. The proportional counter background count rate was then about 80 counts/minute, which was typically two orders of magnitude less than the x-ray count rate.

The proportional counter gas was pure methane at 50-Torr pressure providing 89% absorption of the oxygen-K x-rays in the proportional counter. The aluminum-K x-rays (1.5 keV), which were also produced by proton bombardment of the aluminum oxide targets, were absorbed with only 10% efficiency, and since their rate of production was only 4% of that of oxygen-K x-rays production, their effect on oxygen-K x-ray detection was negligible. The proportional counter voltage was 1250 volts.

For comparison with previous work, aluminum-K x-rays produced by bombardment of pure aluminum targets were also detected. In this case the proportional counter window was 0.005-inch aluminum foil, also backed by nickel mesh clamped in place by a brass collimator. Essentially complete absorption of the aluminum-K x-rays in the proportional counter was provided by 90% argon, 10% methane counter gas at atmospheric pressure. The proportional counter voltage was 2200 volts.

The proportional counter pulses (1-microsecond risetime, 100-microsecond duration) were amplified; sent to a single-channel pulse-height analyzer for low-level and high-level discrimination; and counted by an electronic scaler, gated by the target current integrator.

The discriminator levels were set to remove low energy

electronic noise and high energy background pulses. Monitoring of levels in relationship to the main peak was accomplished using a multichannel pulse-height analyzer, gated by the single-channel analyzer. Typical pulse-height spectra are shown in Figure 8-6.

8.2.5 Target Preparation

The targets, as purchased,* were polycrystalline, high-purity (99.9999%) aluminum wafers, 3/4 inch in diameter by 1/4 inch in thickness. Both sides of the wafers were spark-planed to provide flat, parallel ($\pm$1/2°) surfaces, reducing the thickness to 3/16 inch.

The targets were mechanically polished with one-micron diamond paste on a rotating felt wheel. They were then electro-polished according to the procedure outlined by Tegart.[T1] The electropolishing solution consisted of 262 ml of acetic anhydride, 138 ml of perchloric acid, and 2 gm of aluminum powder. To minimize the explosive hazard while mixing, the perchloric acid was added drop-by-drop, maintaining the temperature of the stirred solution below 25° C.

The targets were suspended in the electropolishing solution by aluminum wire, wrapped around their circumferences, and rotated at six rpm. Polishing was accomplished at 25 v, 10 ma/cm^2 for 30 minutes. A 500-ml aluminum beaker was used for the cathode, and the temperature of the solution was maintained at 23 $\pm$ 2° C. The targets were rinsed by a fast stream of tap water, followed by immersion in distilled water. The resultant, mirror-like,

---

*Cominco American Inc., Spokane, Washington

surfaces were examined with an optical microscope. Small pits of less than five-micron diameter were observed but covered less than 0.25% of the surfaces.

Anodic oxidation of aluminum in suitably buffered electrolytes produces a uniform, highly protective oxide layer.[Y5] If the anodization is performed at constant voltage, the film thickness approaches an almost constant value after a few minutes. This value varies linearly with applied voltage up to several hundred volts (approximately 13 Å/volt).[H5] Lewis and Plumb [L1] showed that a hot aqueous solution of phosphoric acid and chromium trioxide will readily dissolve the oxide layer, replacing it with a mixed oxide film 10 - 20 Å thick.

To remove surface impurities and provide reproducibly flat surfaces, the aluminum wafers were anodized in an aqueous solution of 3% ammonium citrate at 100 v for 10 minutes. The targets were suspended by aluminum wire, and the cathode was a 500-ml aluminum beaker. They were then immersed for 10 minutes in an aqueous solution of othophosphoric acid (50 gm/liter), and chromium trioxide (30 gm;liter), maintained above 90° C. Davis, Friesen, and McIntyre [D2] showed that this treatment was adequate to remove even a 100-v film. The targets were alternately anodized and stripped three time followed by a distilled water rinse and ethyl alcohol rinse.

At this state in target preparation, the targets were used for characteristic aluminum K-shell x-ray yield measurements. Exposure to air was limited to two hours before target chamber evacuation to minimize air-induced oxidation. According to

Hass,[H5] the oxide film formed on aluminum exposed to air for two hours is about 10 Å thick.

For the characteristic oxygen K-shell x-ray yield measurements, a further anodic oxidation step was necessary. After the pre-anodizing and stripping operations, the targets were anodized for 10 minutes at voltages ranging from 0 to 300 volts. The electrolyte was maintained at 25 $\pm$ 0.5° C, and the initial current density was limited to 150 ma/cm^2. After 10 minutes the current density had decreased to about 10 μa/cm^2, corresponding to a film growth rate of less than 0.5% per minute. A final distilled water rinse and ethyl alcohol rinse was again used, and air-exposure was limited to 2 hours.

The anodization procedure followed here was identical to that used by Davies, et al.[D2] Using neutron activation analyses, they accurately determined the slope of oxide film thickness as a function of anodization voltage (0.25 μg aluminum/cm^2 volt or to 0.222 μg oxygen/cm^2 volt). Additional measurements were made to verify stoickiometry of the alumina film.

8.3 Characteristic Aluminum K-Shell X-ray Yield Measurements

The characteristic aluminum K-shell x-ray yields from three electropolished thick targets of aluminum bombarded by 40- to 100-keV protons were measured. The experimental observable was $N(E_o)$, the number of x-rays per μC detected by the proportional counter, where E_o was the proton energy. Corrections for geometry, x-ray absorption in the alumina windows, and proportional counter detection efficiency were necessary to give the thick target x-ray yield $I_T(E_o)$ (x-rays/proton),

$$I_T(E_o) = (a\Lambda/TA)N(E_o) \quad , \tag{8-1}$$

where $a = 1.60 \times 10^{-13}$ μC/proton, $\Lambda = 4\ R^2/r^2$ is the geometrical correction factor [R(cm) = distance from the target to the proportional counter, r(cm) = radius of the proportional counter window as defined by the x-ray collimator], T is the total transmission of the x-ray windows, and A is the absorption in the proportional counter.

The geometrical correction factor Λ was calculated to be 6.75×10^4. Window transmission was measured by inserting absorbers identical to the x-ray windows into the x-ray beam. Then

$$T = \frac{N(E_o)\,[\text{without absorbers}]}{N(E_o)\,[\text{with absorbers}]} = 0.218 \pm 2\%.$$

Since the counter represented nine absorption lengths for the aluminum-K x-rays, A = 1.00. Therefore,
$I_T(E_o) = (4.95 \times 10^{-8} \pm 2\%)N(E_o)$.

The aluminum thick target yield results are given in Figure 8-7, along with those of Khan, Potter, and Worley.[K5] The agreement is generally within 10%, less than their stated error of ± 15%. The results represent the average yields measured from the three electropolished targets. Individual target yields agreed with the average to ± 5%.

The characteristic aluminum K-shell x-ray yield measurements clearly proved the experimental apparatus. In addition, the importance of smooth, fine polycrystalline target surfaces to

accurate polycrystalline thick target x-ray yield measurements was indicated.

8.4 Characteristic Oxygen K-Shell X-ray Yield Measurements

8.4.1 Theory

With straight proton trajectories, and assuming isotropic x-ray emission, a uniform aluminum oxide target, and a mathematically plane target surface with the surface normal oriented 45° with respect to both the proton beam and the direction of x-ray detection, the characteristic oxygen K-shell x-ray yield I (x-rays/proton) is given by: [M6]

$$I(E_o,t) = n \int_o^t \exp(-\mu_a x) \quad \sigma[E(x)]\, dx, \tag{8-2}$$

where

E_o = initial proton energy in keV,

t = oxygen surface density in μg oxygen/cm^2,

n = number of oxygen atoms per μg of oxygen,

μ_a = mass absorption coefficient of aluminum oxide for characteristic oxygen K-shell x-rays in cm^2/μg of oxygen,

σ = characteristic oxygen K-shell x-ray production cross section in cm^2/oxygen atom,

$E(x)$ = proton energy in keV after traversing x μg of oxygen/cm^2.

For small t, Equation (8-2) reduces to:

$$I(E_o,t) \simeq n\, \sigma(E_o)\, t. \tag{8-3}$$

The partial derivative of Equation (8-2) with respect to t, evaluated at t = 0, gives the characteristic oxygen K-shell x-ray

production cross section:

$$\sigma(E_o) = \frac{1}{n} \left[\frac{\delta I(E_o,t)}{\delta t} \right]_{t = 0}. \tag{8-4}$$

Equation (8-2) can be transformed into a function of proton energy alone through the stopping power

$$S(E) = - \frac{dE}{dx} . \tag{8-5}$$

In particular, as t approaches the proton range, E approaches zero, and the thick target oxygen K-shell x-ray yield is

$$I_T(E_o) = n \int_o^{E_o} \frac{\sigma(E)}{S(E)} \exp \left[\mu_a \int_{E_o}^{E} \frac{dE'}{S(E')} \right] dE. \tag{8-6}$$

Differentiating Equation (8-6) with respect to E_o gives the stopping power

$$S(E_o) = \left[\frac{dI_T(E_o)}{dE_o} \right]^{-1} \left[n\sigma(E_o) - \mu_a I_T(E_o) \right] . \tag{8-7}$$

From Equation (8-3), the oxygen-K x-ray yield for thin targets should vary approximately linearly with oxygen surface density, and the initial slope gives the characteristic oxygen K-shell x-ray production cross section by Equation (8-4). Then measurements of thick-target oxygen-K x-ray yields as a function of proton energy enable calculations of the stopping power from Equation (8-7).

8.4.2 Results

The characteristic oxygen K-shell x-ray yields from eight electropolished and anodized aluminum targets bombarded by 20- to 100-keV protons were measured. The anodization voltages varied from 0- to 300-volts.

The x-ray yields were calculated from the experimentally observed number of counts per μC using Equation (8-1). The geometrical correction factor was 1.13×10^{-5}, and the measured total x-ray window transmission was 0.177 ± 1%. The proportional counter absorption was determined to be 0.886 ± 1% by measurement of the x-ray yield as a function of counter pressure and using the equation:

$$A = 1 - e^{-cp} , \tag{8-8}$$

where c = constant and p = pressure. Then,

$$I(E_o,t) = (1.15 \times 10^{-7} \pm 2\%)\ N(E_o,t).$$

The experimental results are given in Figures (8-8 and 8-9). The anodization voltage was converted to t (μg oxygen/cm^2) using the conversion factor: 0.222 μg oxygen/cm^2 volt. The close approach to asymptotic values of the yield, which correspond to thick-target bombardment occurs at lower oxide thicknesses as the proton energy is decreased, due to decreasing proton ranges. The close agreement of the thick-target x-ray yields from the two 300-volt targets (± 1%) confirmed the reliability of target preparation. Uniformity of the oxide was investigated by thick-target x-ray yield observations as the targets were

rotated $\pm$ 2°; the x-ray yields were constant to $\pm$ 1%.

The thin-target results are shown in Figure 8-10. As expected from Equation (8-3), the thin-target x-ray yield varies approximately linearly with oxygen surface density. The effective anodization voltage (2.8 volts) required to account for the observed oxygen surface density at zero applied voltage is larger than the value (1.8 volts) measured by Davies, et al.[D2] This is attributed to the estimated 10 Å of oxide formed during the two-hour air exposure, since 10 Å corresponds to an anodization voltage of approximately one volt.[H5] The slopes at 5-volt anodization voltage were determined. Using these values as approximate initial slopes, the approximate value of the characteristic oxygen K-shell x-ray production cross section $\sigma(E_o)$ was calculated using Equation (8-4).

The thick-target x-ray yield as a function of proton energy (Figure 8-11 and Table 8-1) then permitted calculation of the approximate stopping power $S(E_o)$ using Equation (8-7); μ_a was 7.7×10^{-3} $cm^2/\mu g$ of oxygen, as calculated from x-ray transmission measurements of the aluminum oxide windows.

With the stopping power approximately known, the slopes at 5-volt anodization voltage were corrected (approximately 5%) to give the initial slope; $\sigma(E_o)$ and $S(E_o)$ were recalculated. A third iteration produced negligible changes. The final characteristic oxygen K-shell x-ray production cross section is given in Figure 8-12 and Table 8-1, and the stopping power for low-energy protons in aluminum oxide is presented in Figure 8-13.

The x-ray yield as a function of anodization voltage or

oxygen surface density at 100-keV proton energy is presented in Figure 8-14. The curve represents numerical integration of Equation (8-2) based on the characteristic oxygen K-shell x-ray production cross section and stopping power results. These results were determined by only the initial slopes and asymptotic values of the oxygen-K x-ray yields as a function of anodization voltage. All data in Figure 8-14 agree with the numerical integration curve to within 3%.

The standard deviations of the oxygen-K x-ray yield measurements resulted from standard deviations of x-ray counting statisitics (2% for 50- to 100-keV proton energies, increasing to 5% at 20 keV), integrated target current measurements (1%), x-ray window transmission measurements (1%), and proportional counter absorption measurements (1%). The calculated standard deviations of the oxygen-K x-ray yield measurements are 3% for 50- to 100-keV proton energies, increasing to 6% at 20-keV proton energy.

The standard deviations of the oxygen K-shell x-ray production cross section results, as shown in Figure 8-12, are 5% for the 50- to 100-keV proton energy range, increasing to 7% for 20-keV protons. The stopping power result given in Figure 8-13 has a standard deviation of 7% from 50- to 100-keV, which increases to 10% at a proton energy of 20 keV. The increased errors, as compared to the x-ray yield measurement errors, were primarily due to an estimated 2.5% error in converting anodization voltage to oxygen surface density.

An additional thick aluminum oxide target was investigated for radiation damage effects on the x-ray yield. The yield for

100-keV proton bombardment was constant to $\pm$ 1% until the target had been bombarded by 6×10^{16} protons/cm^2, at which integrated current the x-ray yield decreased 1%. A 2% reduction in yield occurred at 1.4×10^{12} protons/cm^2. Primak and Luthra have observed the onset of blistering of magnesium oxide bombarded by 140-keV protons at 6×10^{17} protons/cm^2. The observed x-ray yield reductions may have been caused by a similar effect. The targets for the oxygen-K x-ray yield measurements were bombarded by a total of 5×10^{16} protons/cm^2 (40% of this total was accumulated during the 20-keV proton energy x-ray yield measurement). This total integrated current is less than that at which 1% change in x-ray yield was observed.

8.4.3 Discussion

The characteristic K-shell x-ray production cross section decreases monotonically with increasing atomic number Z, due to increasing K-shell binding energy.[M6] The results for oxygen (Z = 8), given in Figure 8-12, are between the previously measured[K5] characteristic K-shell x-ray production cross sections of carbon (Z = 6) and magnesium (Z = 12), consistent with the expected Z dependence. Unfortunately, no satisfactory theoretical results for the interaction of low-energy protons with low Z elements exist.[M6,K5]

The present stopping power result for low-energy protons in aluminum oxide is presented in Figure 8-13, together with calculated values assuming chemical additivity, based on the stopping power of aluminum and oxygen given by Allison and Warshaw.[A8] An error of $\pm$ 10% was assigned these values because of a similar variation in the oxygen stopping power. The agreement

is within experimental error; however, the present data has peaks at 65-keV and 90-keV proton energies, which are not clearly shown in the chemical additivity calculation.

The reported stopping power for aluminum does have a pronounced peak at 7-keV proton energy, and the reported oxygen stopping power has a shallow peak at 90 keV. These proton energies approximately agree with those corresponding to the peaks in the present data. The oxygen stopping power given in Reference A8 was measured by a technique in which only proton energy losses in interactions with practically free electrons were observed. The total stopping power, as measured here, also includes interactions with tightly bound electrons, which apparently lead to more pronounced peaking.

The agreement of the present stopping power results with those of Allison and Warshaw [A8] indicates that the technique developed in this work is valid. Since this technique does not depend on self-supporting thin targets, it may provide a means of obtaining more stopping power measurements in the low-energy proton range.

The close agreement of the experimental characteristic oxygen K-shell x-ray yields at 100-keV proton energy as a function of target thickness with the numerical integration results of Equation (8-2), as indicated in Figure 8-14, tend to confirm the assumptions used to derive Equation (8-2). The correlation of oxygen-K x-ray yield with oxygen surface density also illustrates the capability of measuring oxygen surface densities to less than 1.0 μg of oxygen/cm^2. The lower limit depends on the target

current, efficiency of x-ray detection, and the background count rate. In the present apparatus, 10 microamps of target current and equal x-ray and background count rates correspond to an oxygen surface density of 4×10^{-3} μg of oxygen/cm^2 (1.5×10^{14} oxygen atoms/cm^2 or approximately 0.1 monolayer). Hence, design objective of constructing apparatus capable of sub monolayer oxygen measurement was successfully met.

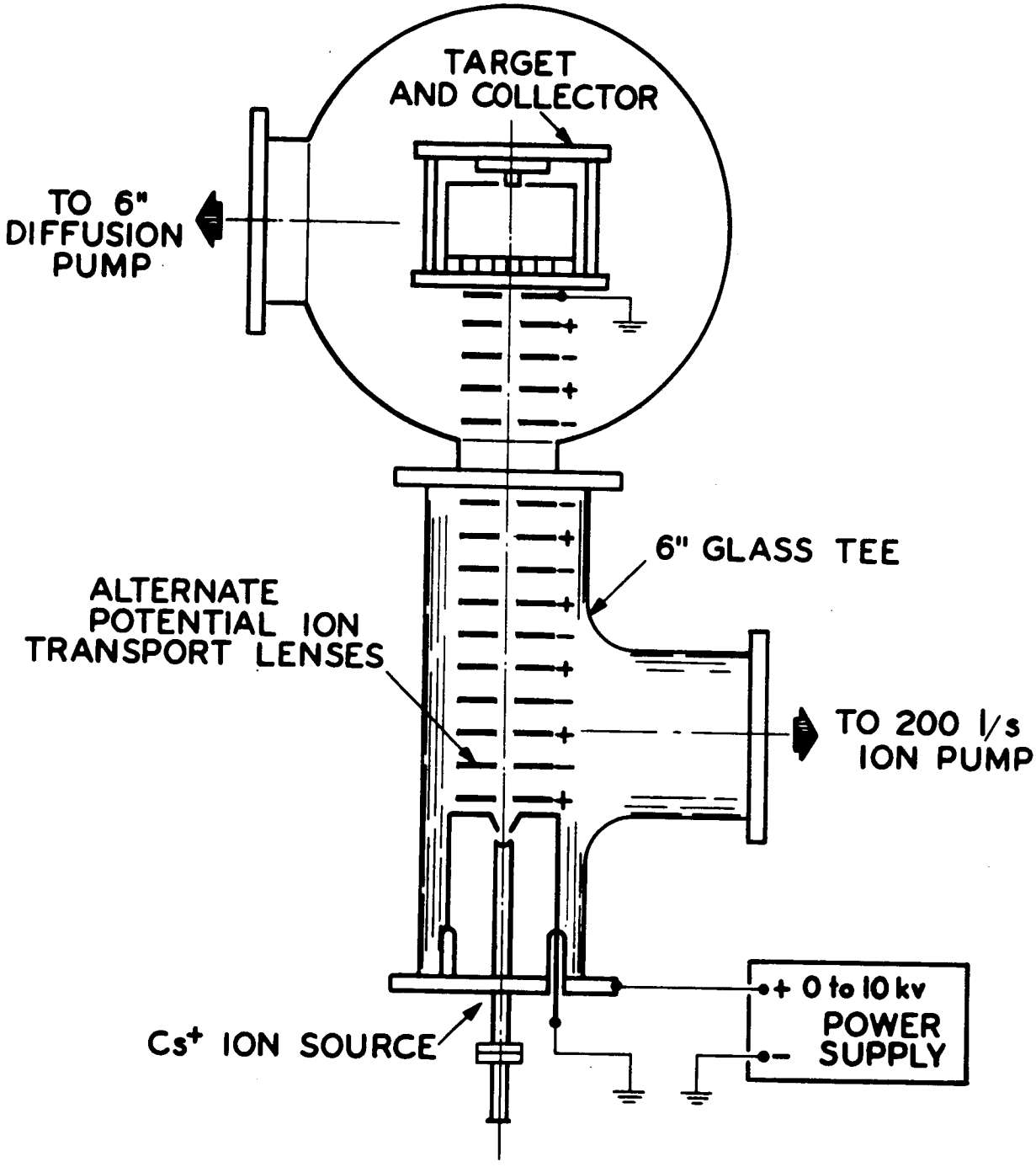

Figure 2-1: Schematic of the combined ion source and target apparatus

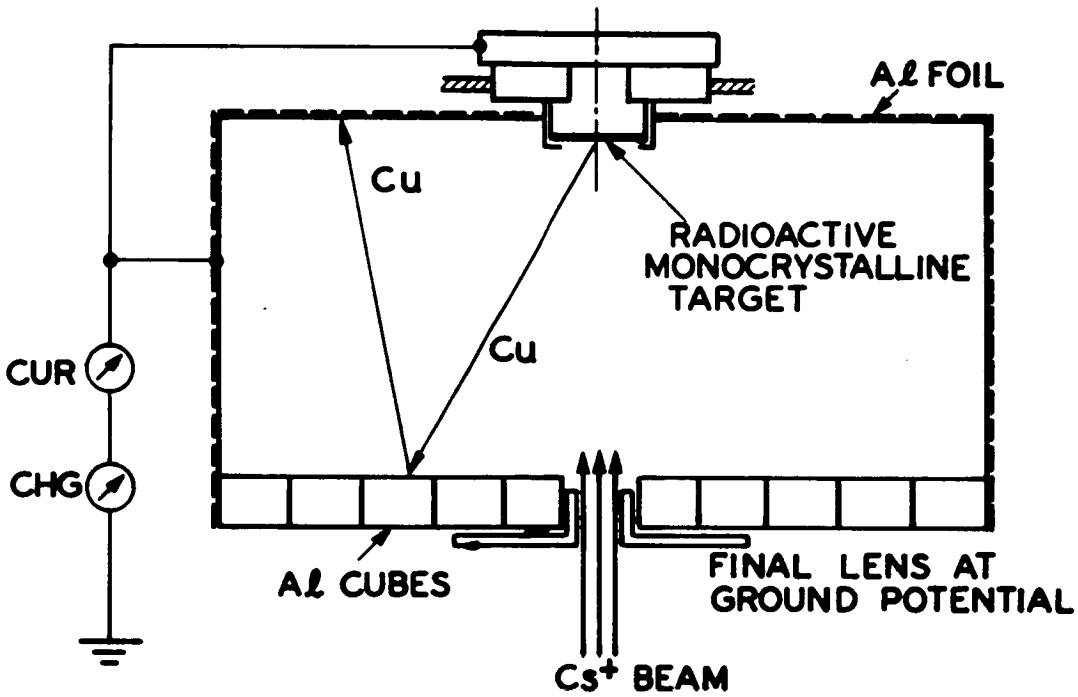

Figure 2-2: Schematic diagram of target-collector assembly for measurement of the yield and angular distribution of sputtered copper. Secondary sputtering of previously collected copper is depicted.

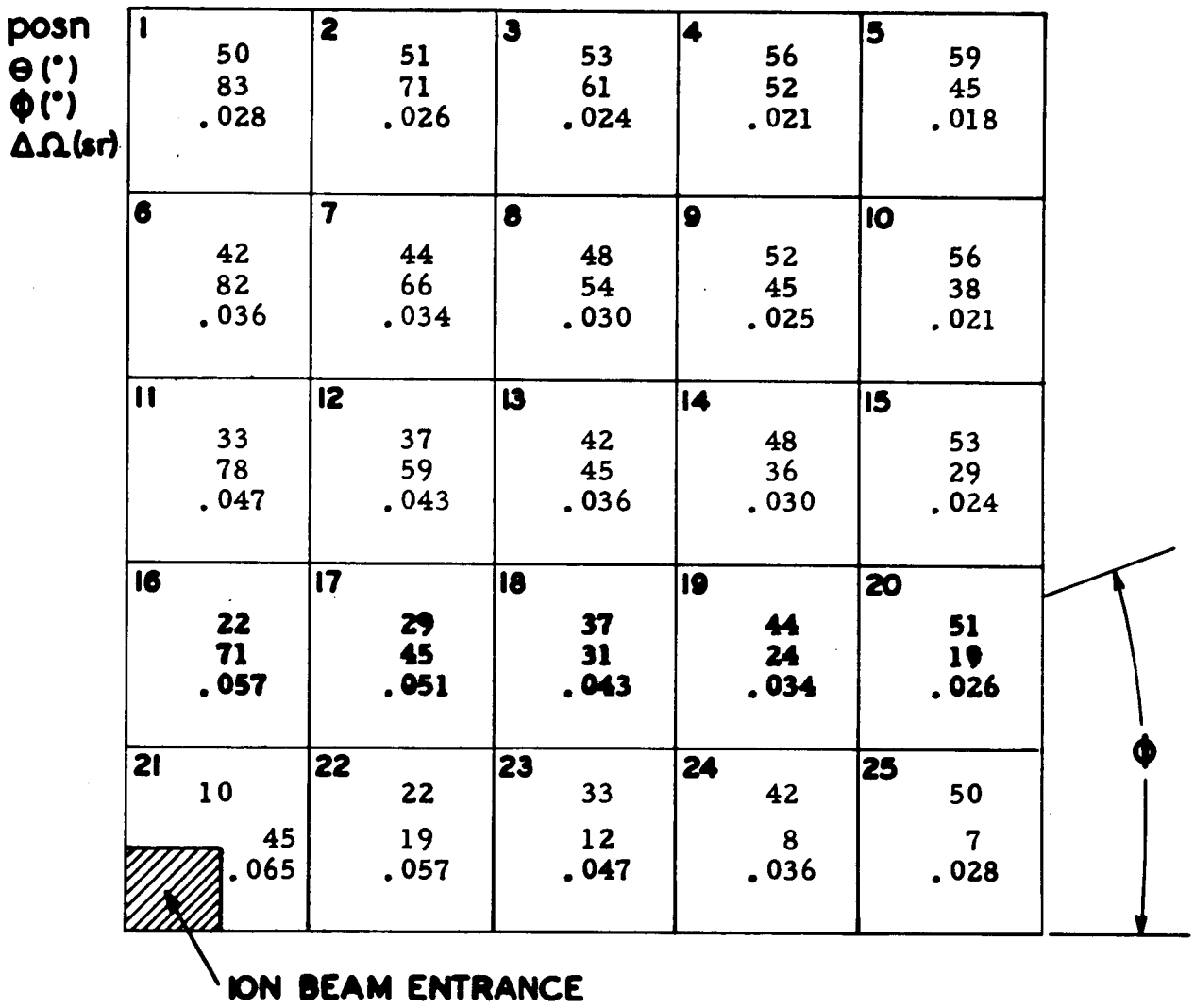

Figure 2-3: Schematic diagram of the angular collector positions for normal bombardment of the (100) surface. θ is the polar angle taken equal to zero along the target surface normal while is the azimuthal angle measured as shown in the surface plane. The solid angle in steradians is presented for each collector position.

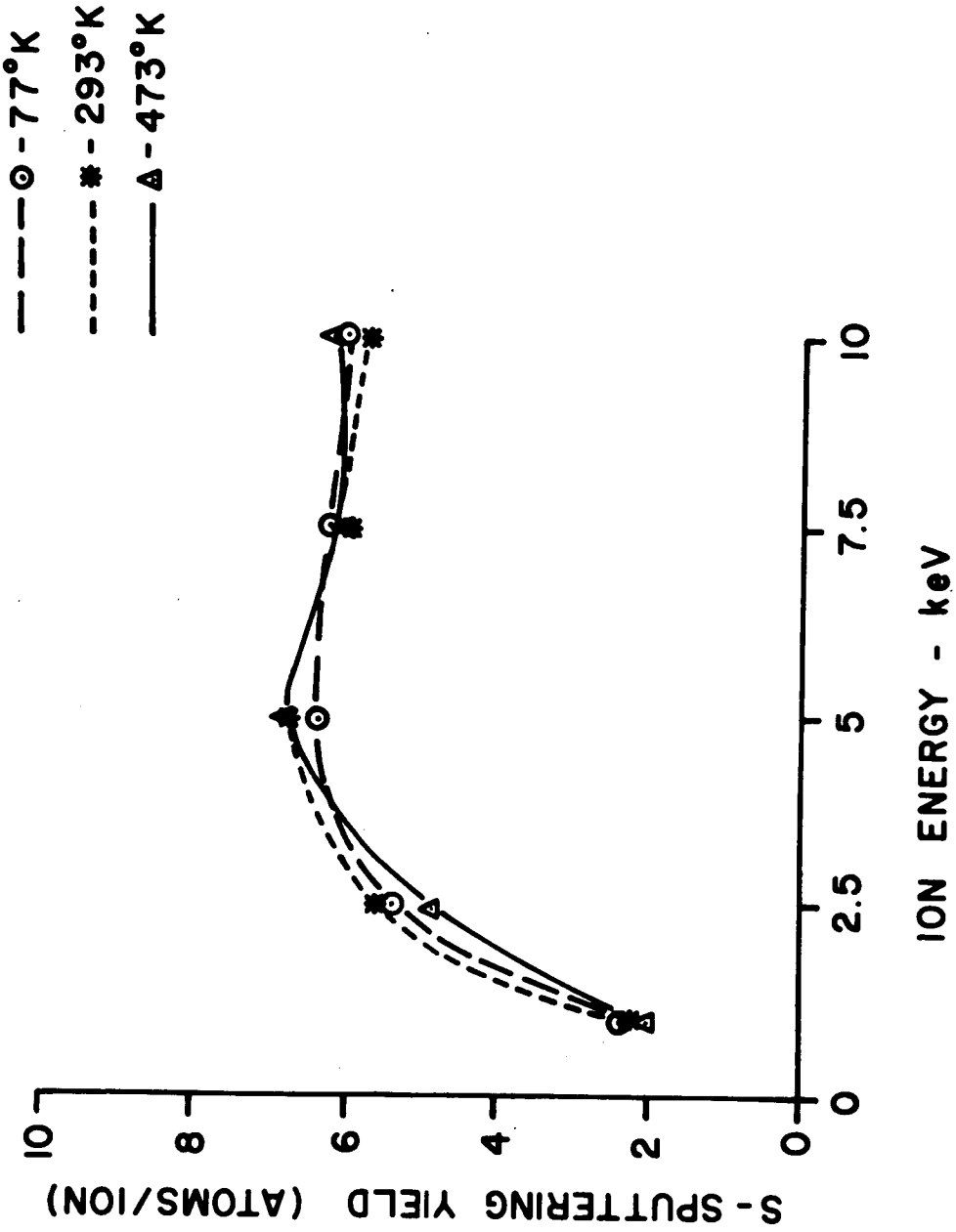

Figure 2-4: Sputtering yield versus incident ion energy for 1- to 10-keV cesium-ion bombardment of monocrystalline copper at 77, 293, and 473° K. The ion beam was normal to the surface and parallel to the [100] direction.

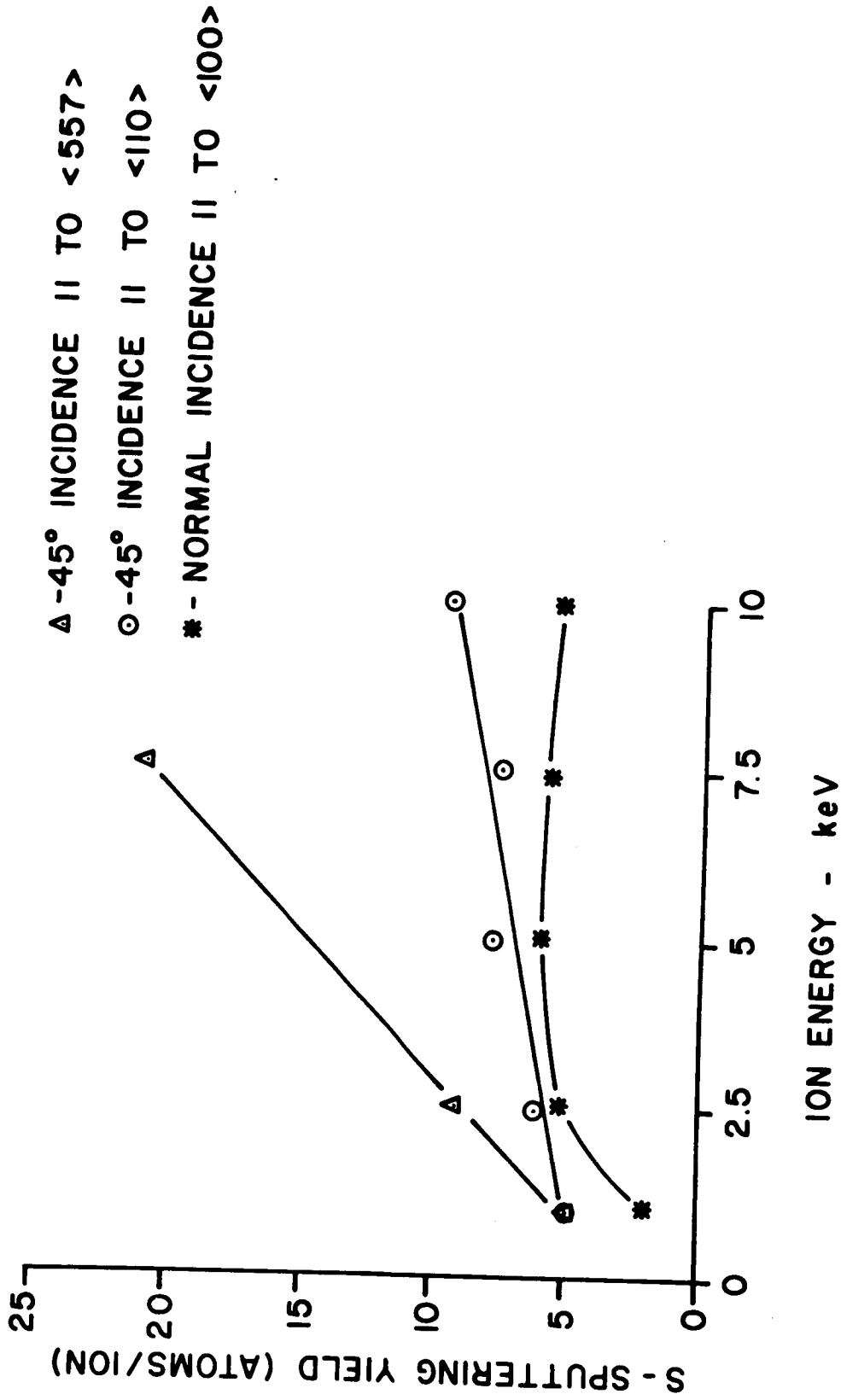

Figure 2-5: Energy dependence of the total sputtering yield for ion beam incident at 45° to the copper normal and parallel to the [110] and [755] crystallographic directions. The yield at normal incidence and 298°K has been included for comparison.

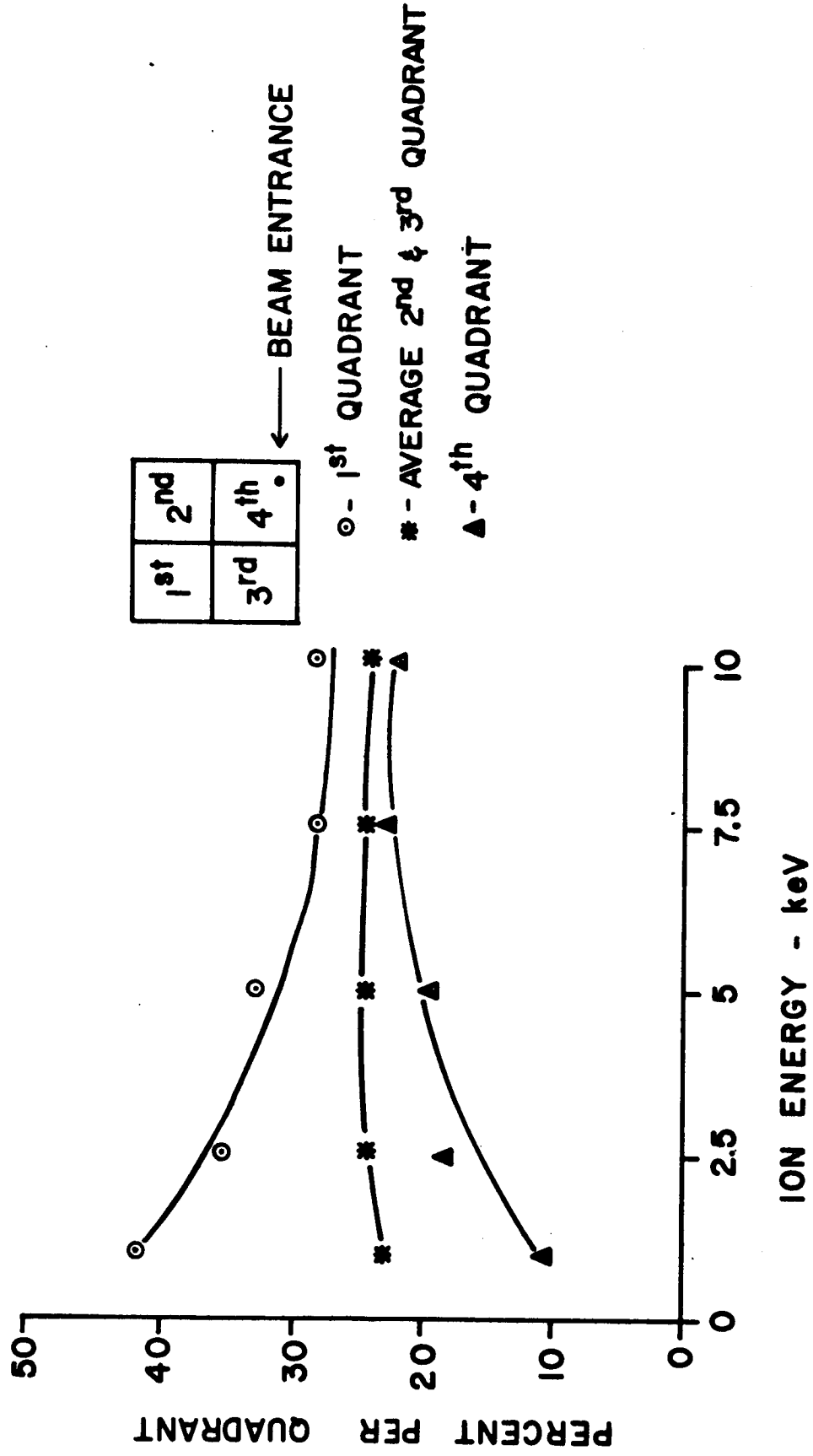

Figure 2-6: Percent yield per collector quadrant for the ion beam incident 45° to the copper surface and parallel to [110] crystallographic direction. The ion beam entered the target-collector chamber along the diagonal of the fourth quadrant as shown in the insert.

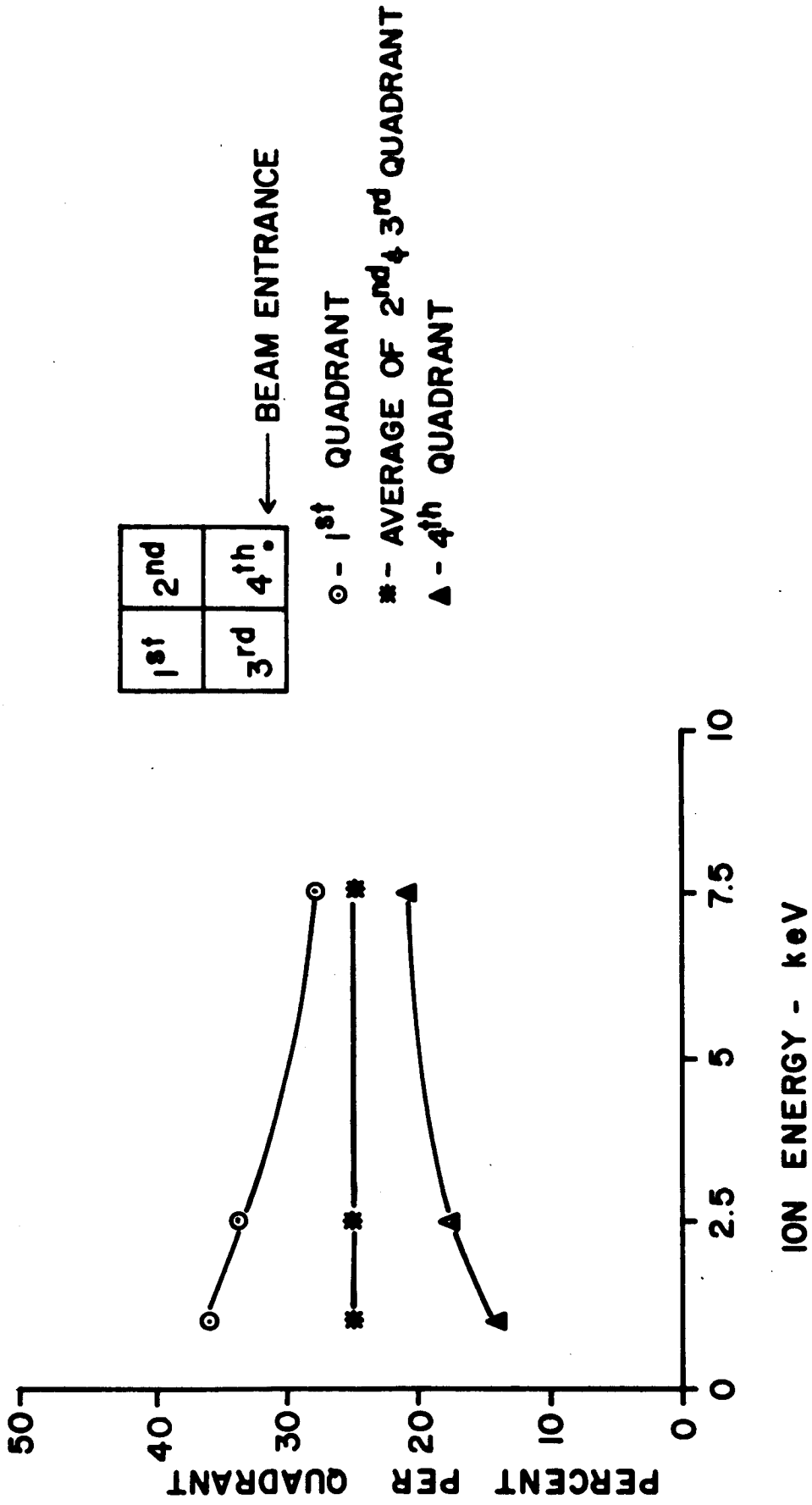

Figure 2-7: Percent yield per collector quadrant for the ion beam incident 45° to the copper surface and parallel to the [755] crystallographic direction.

(Dc5)

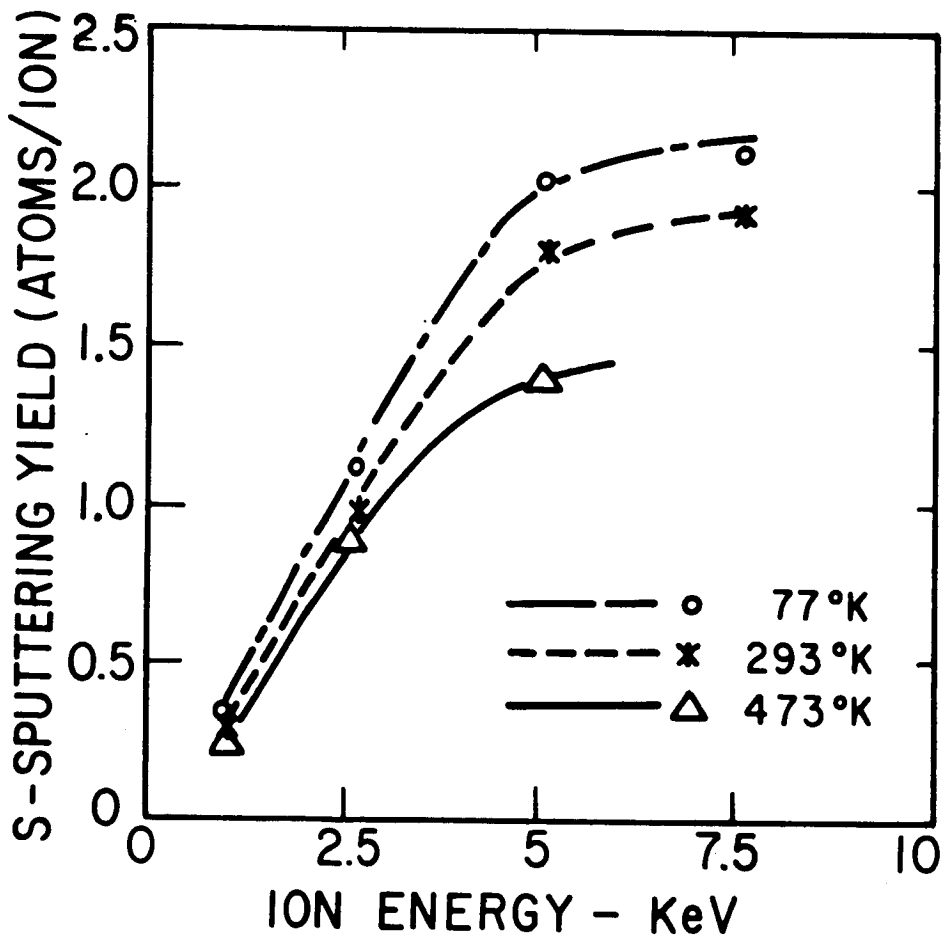

Figure 3-1: Sputtering yield versus incident ion energy as a function of target temperature. Bombardment was normal to the (100) crystallographic face and to the surface.

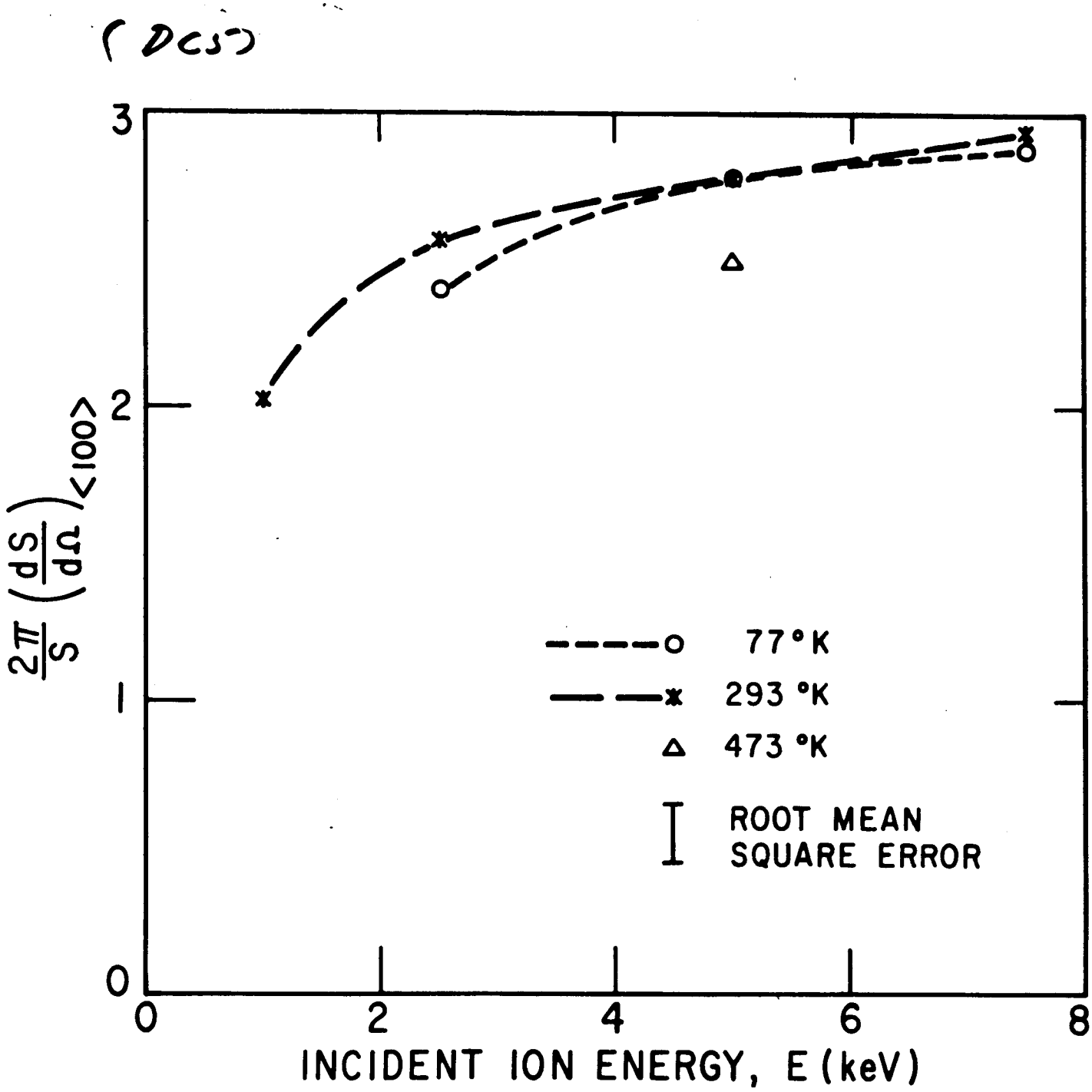

Figure 3-2: Normalized emission $(2\pi/S)$ $(dS/d\Omega)$ in the $\langle 100 \rangle$ direction as a function of incident ion energy and target temperature. The emission is calculated from the radioactivity of four collectors contained in a cone of 14-deg half-angle and located symmetrically about the ion beam entrance and the $\langle 100 \rangle$ direction. Uniform coverage of the collector face is assumed in compensating for loss of sputtered particles through the entrance hole.

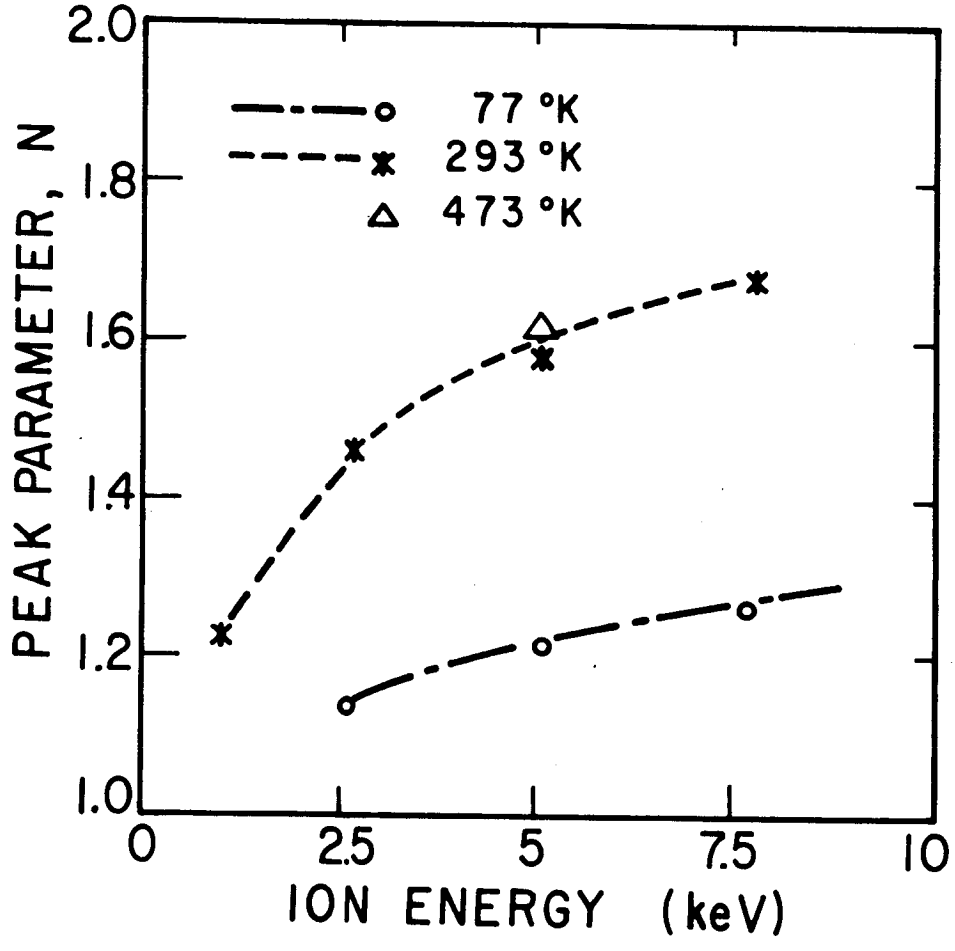

Figure 3-3: Energy and temperature dependence of the peak parameter N.

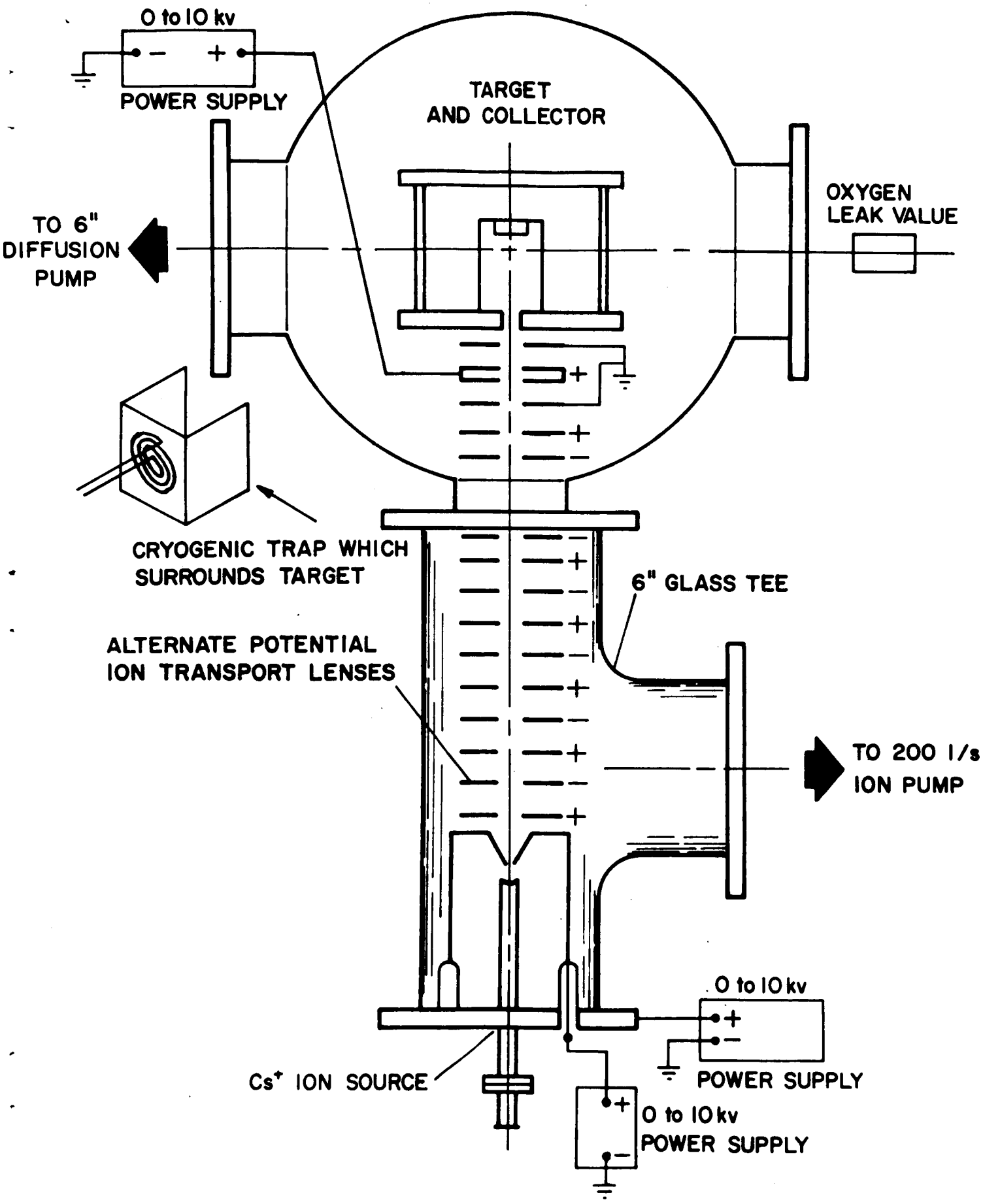

Figure 4-1: Schematic diagram of the combined ion source and target apparatus.

(GM4)

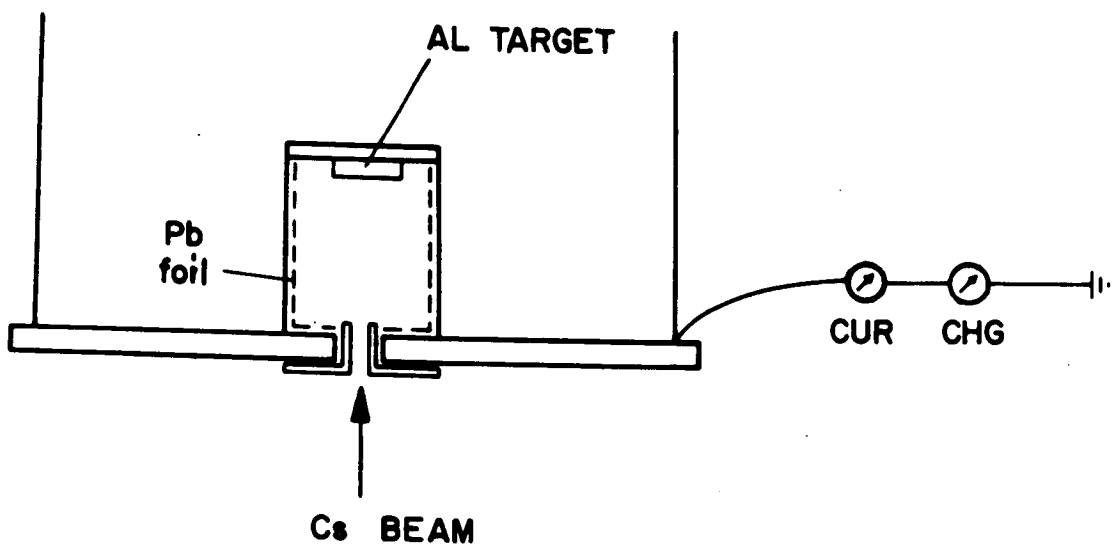

Figure 4-2: Schematic diagram of the target-collector assembly for measurement of the yield of sputtered aluminum.

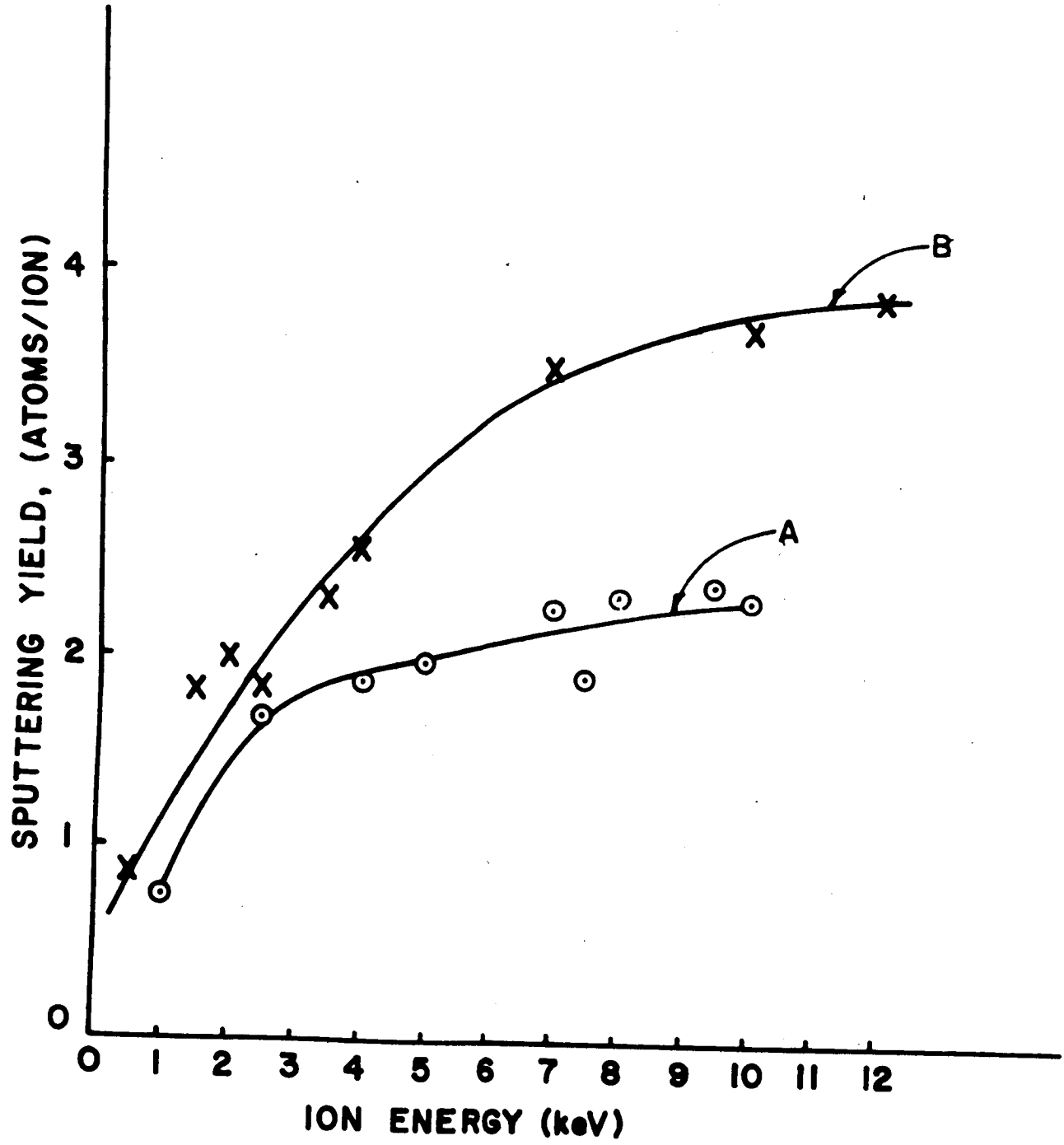

(6-44)

Figure 4-3: Sputtering yield vs. incident ion energy for cesium ion bombardment normal to an aluminum target surface at 20°C. The data of curve (A) are for a (110) surface of a monocrystalline target while the data of curve (B) are those of Daley and Perel who used a polycrystalline target.

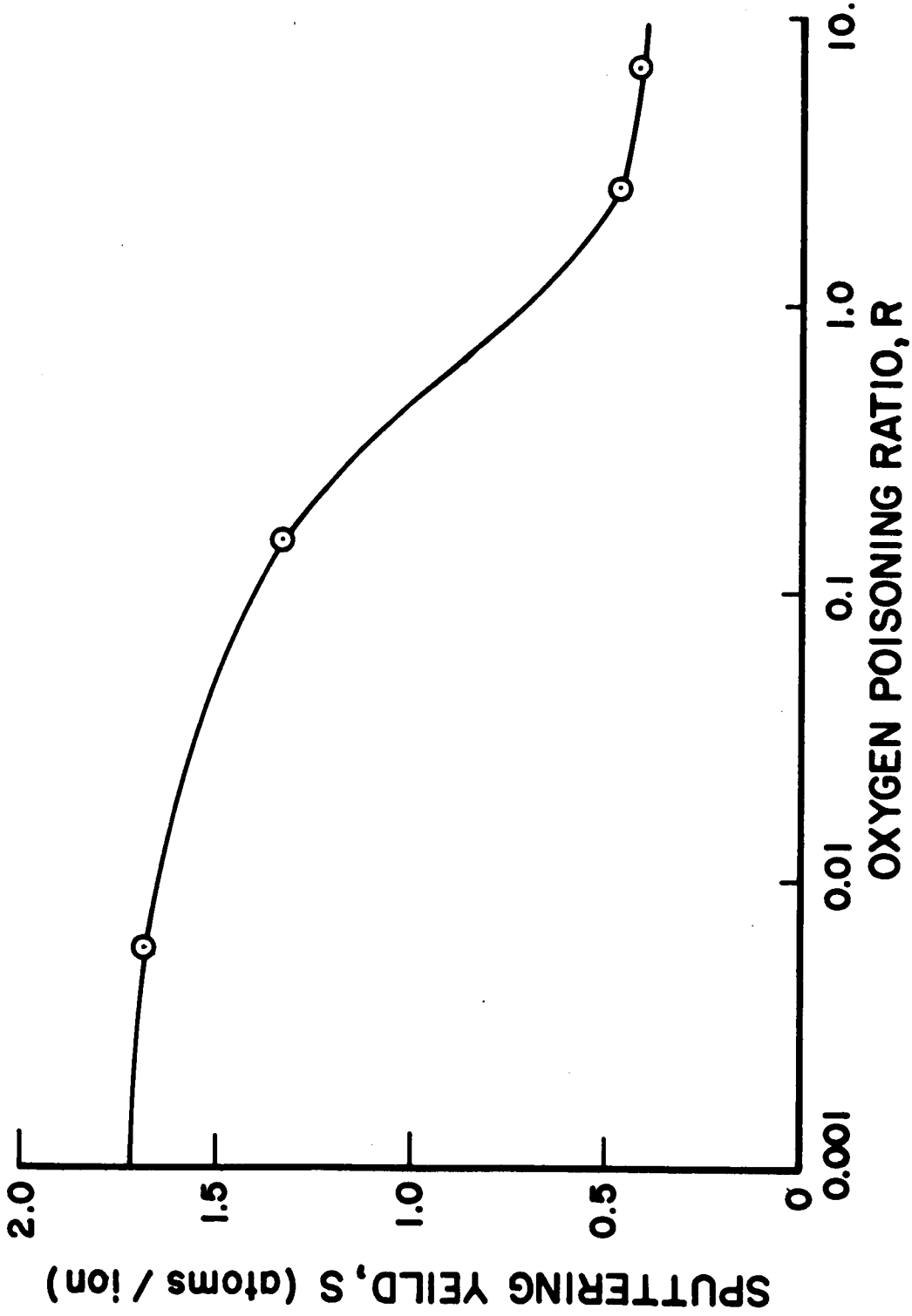

Figure 4-4: Sputtering yield of aluminum vs. oxygen poisoning ratio for 2.5 keV cesium ion bombardment normal to the (110) surface of aluminum at 20°C.

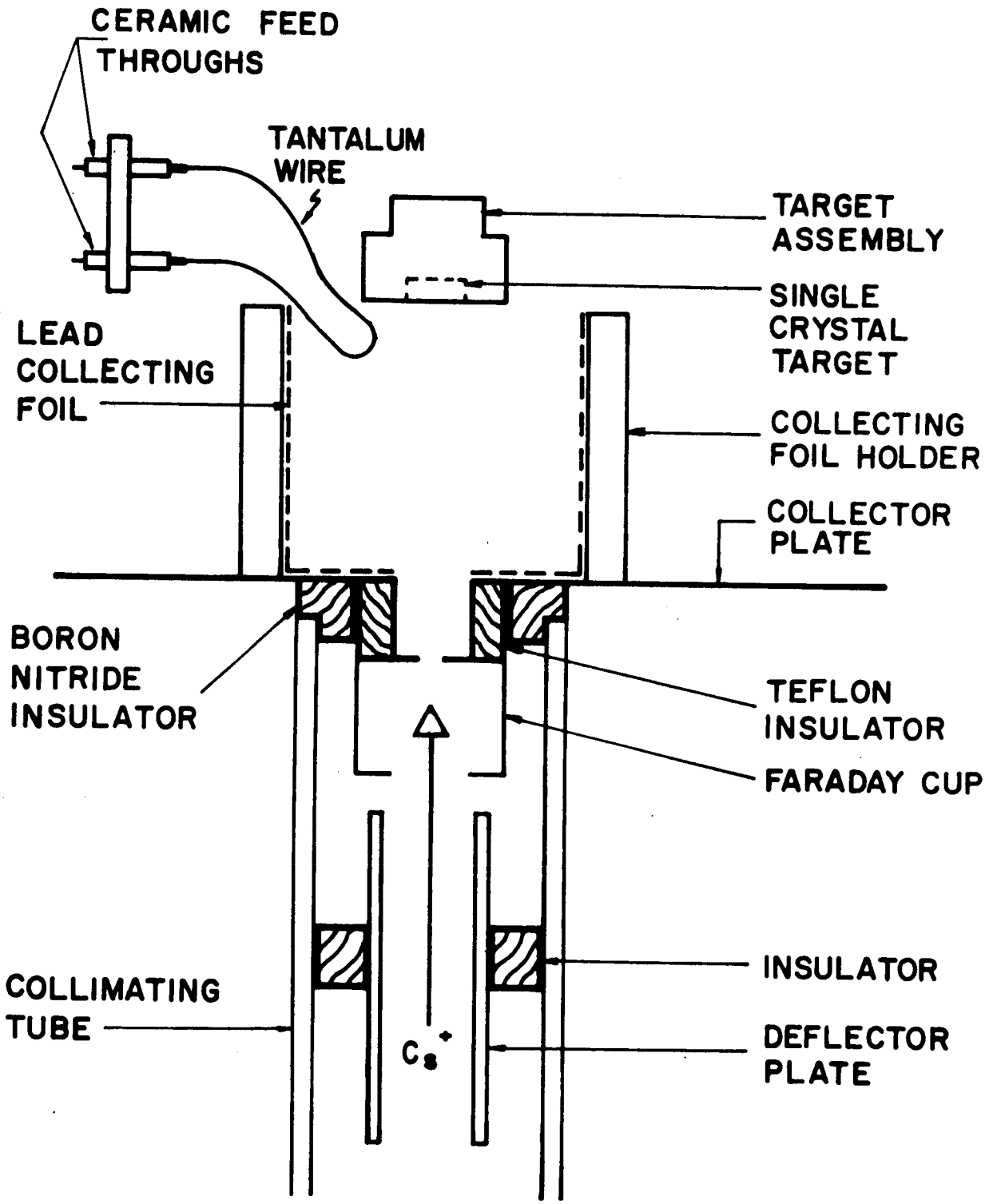

FIGURE 5-1

Schematic of target and collector showing devices for charge neutralization and ion current measurement.

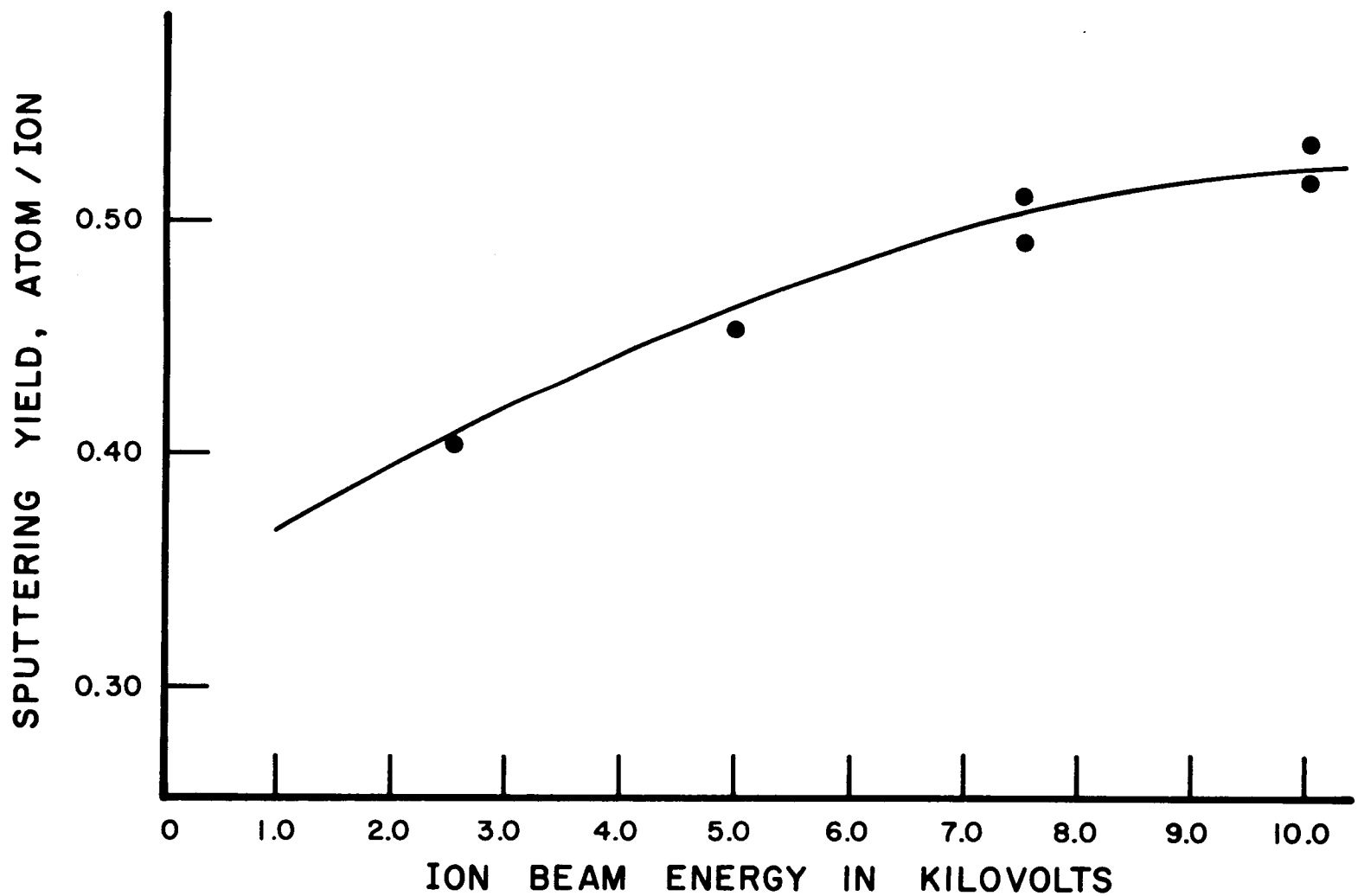

Figure 5-2

Sputtering yield vs. incident ion energy for cesium ion bombardment normal to (001) face of monocrystalline aluminum oxide at 60°C.

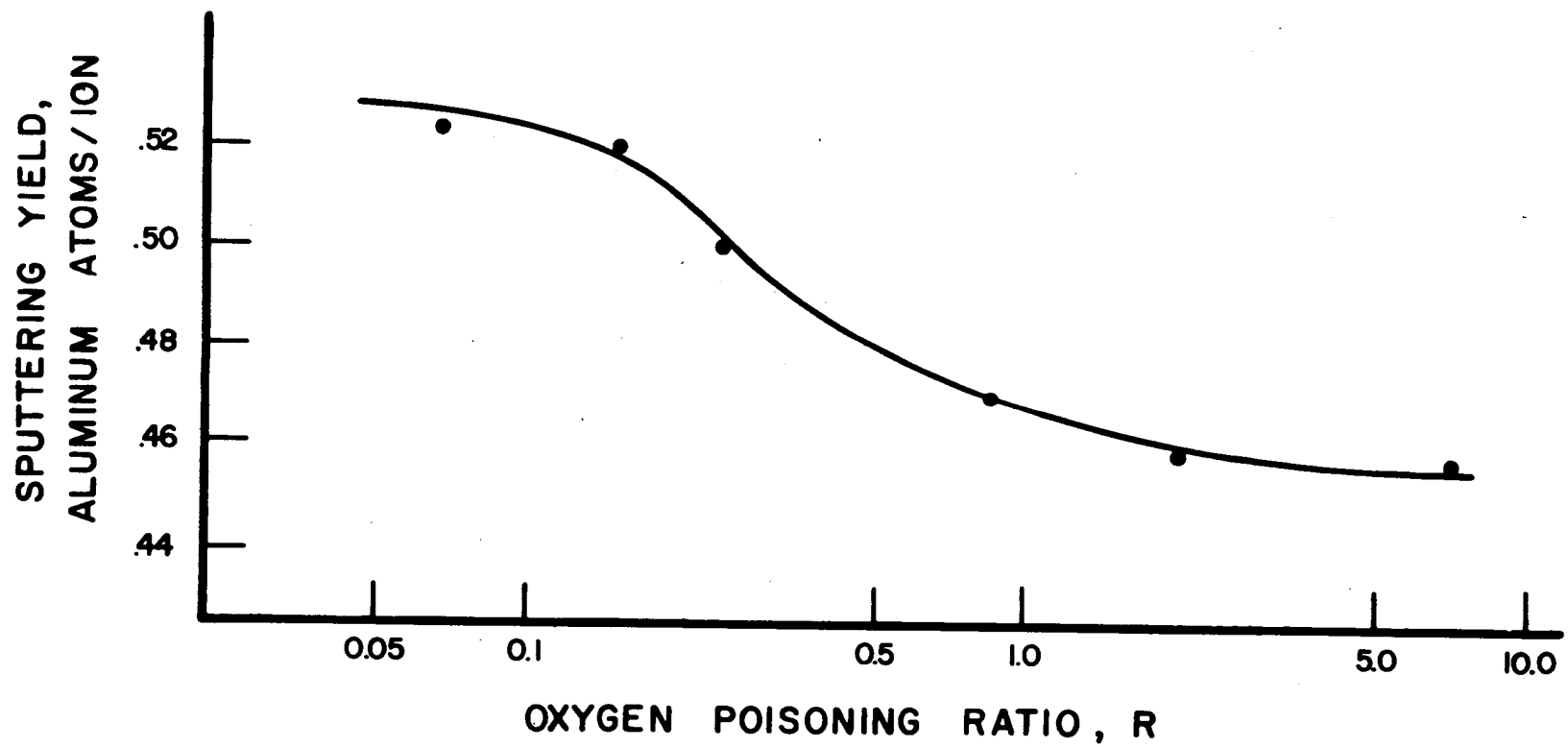

FIGURE 5-3

Sputtering yield vs. oxygen poisoning ratio for 10.0 keV cesium ion bombardment normal to (001) face of monocrystalline aluminum oxide at 60°C. The calculation of the poisoning ratio assumed that for every two aluminum atoms sputtered from the Al_2O_3 lattice, three oxygen atoms were also sputtered.

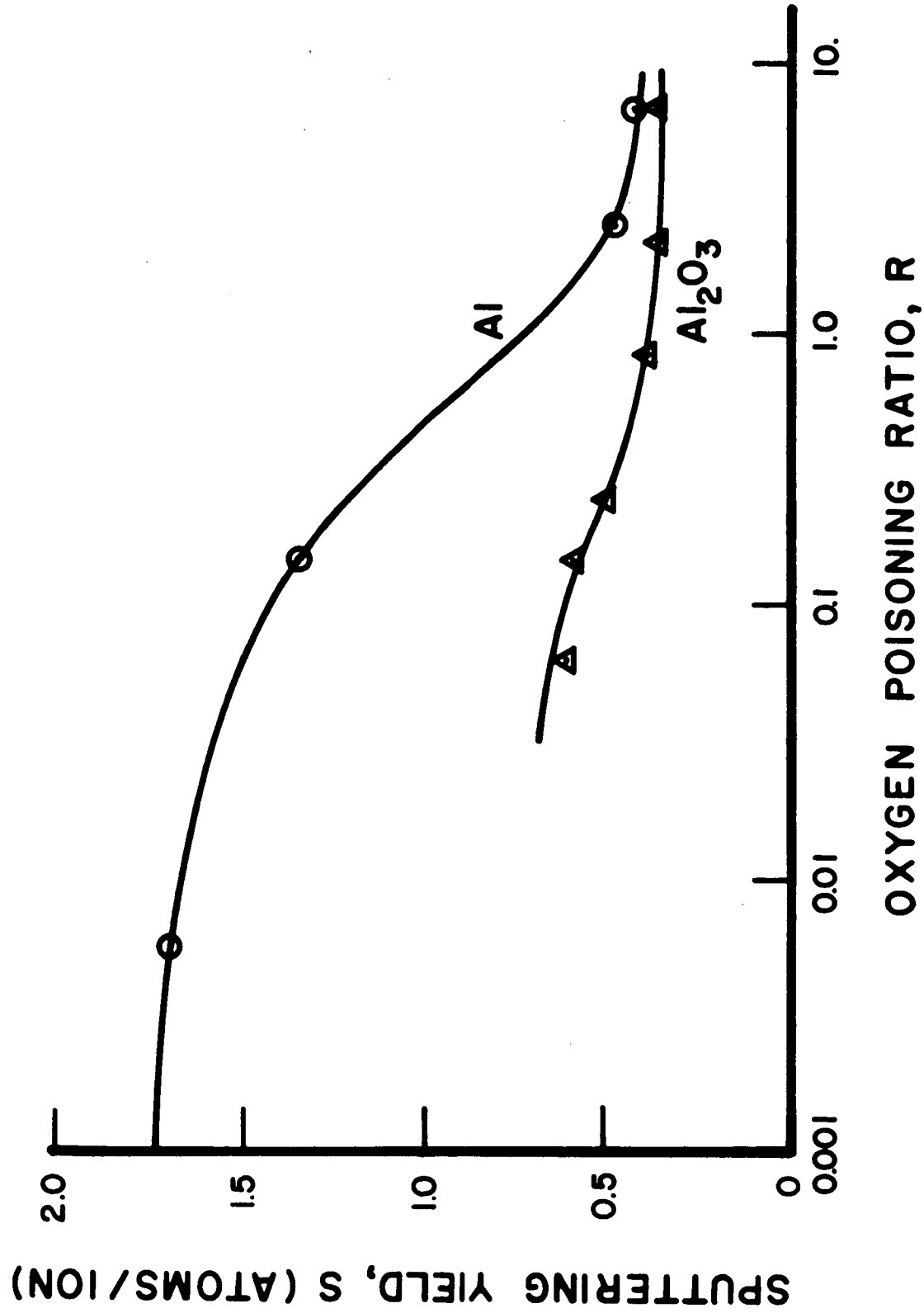

Figure 5-4: Comparison of sputtering yield versus poisoning ratio curves for aluminum and aluminum oxide for 10.0 keV cesium ion bombardment.

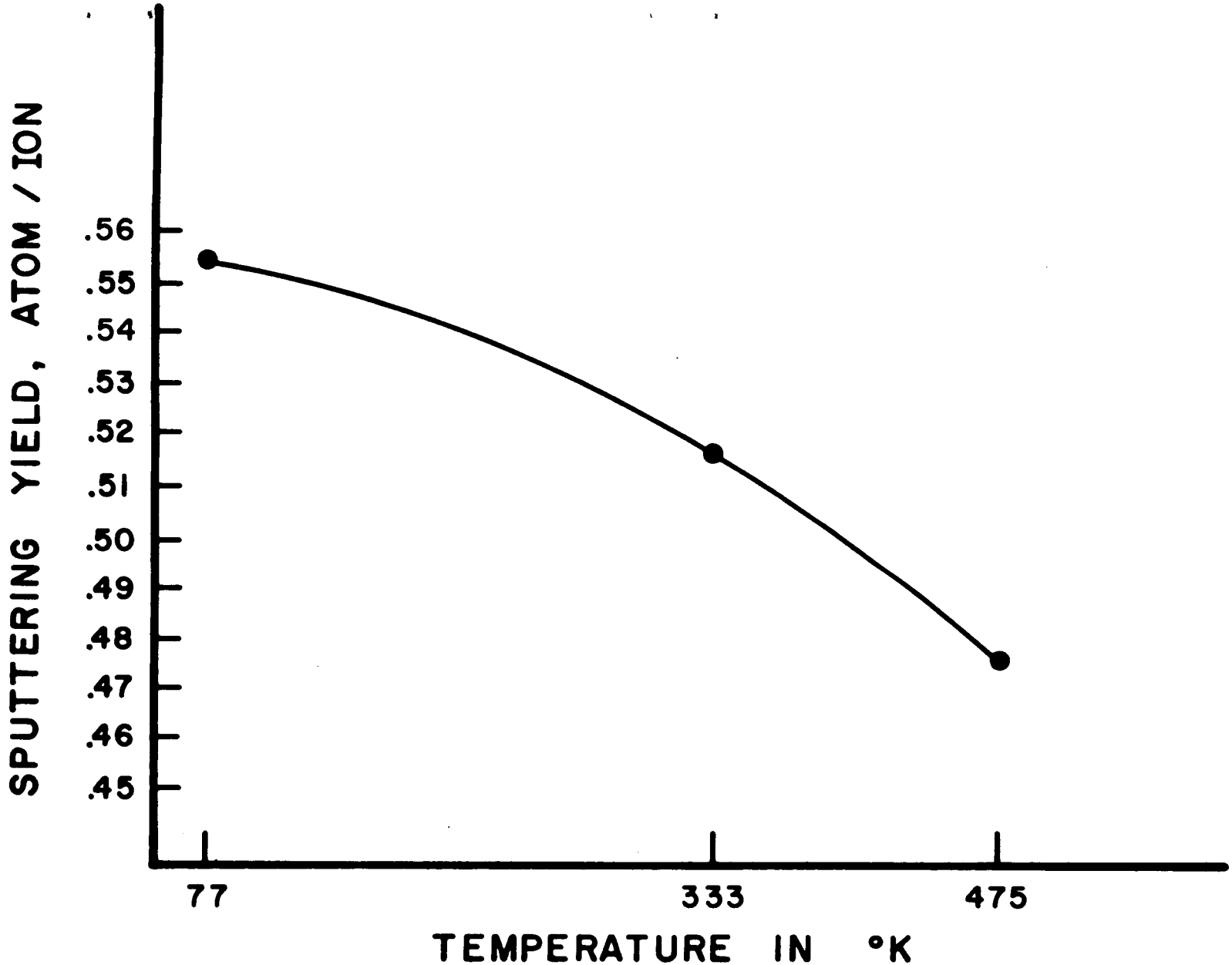

Figure 5-5

Sputtering yield vs. target temperature for 10.0 keV cesium ion bombardment normal to (001) face of monocrystalline aluminum oxide

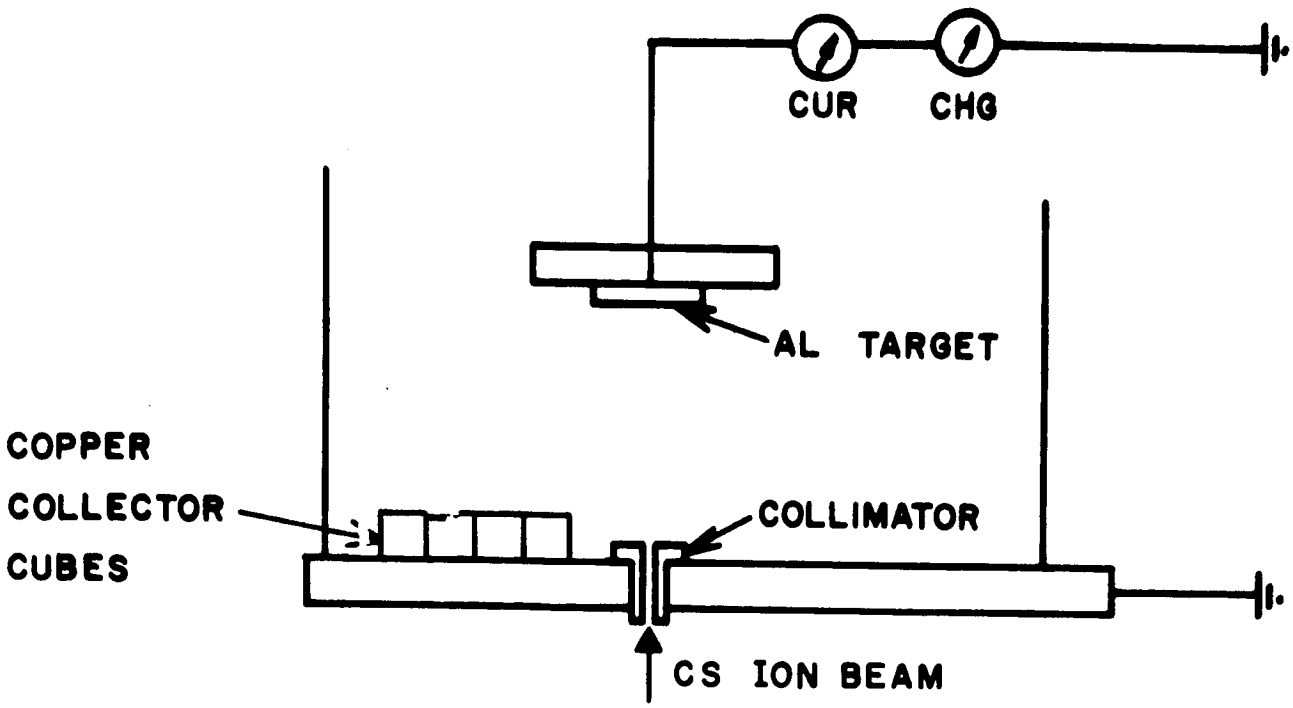

(a)

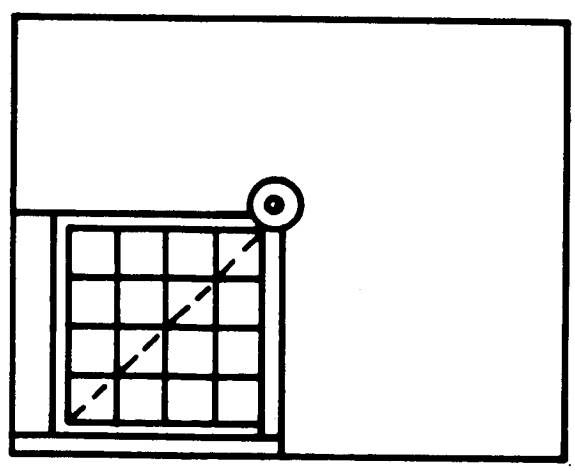

(b)

Figure 6-1

Target and collector assembly with:
(a) side view, (b) top view of collector with plane of analysis shown by dotted line.

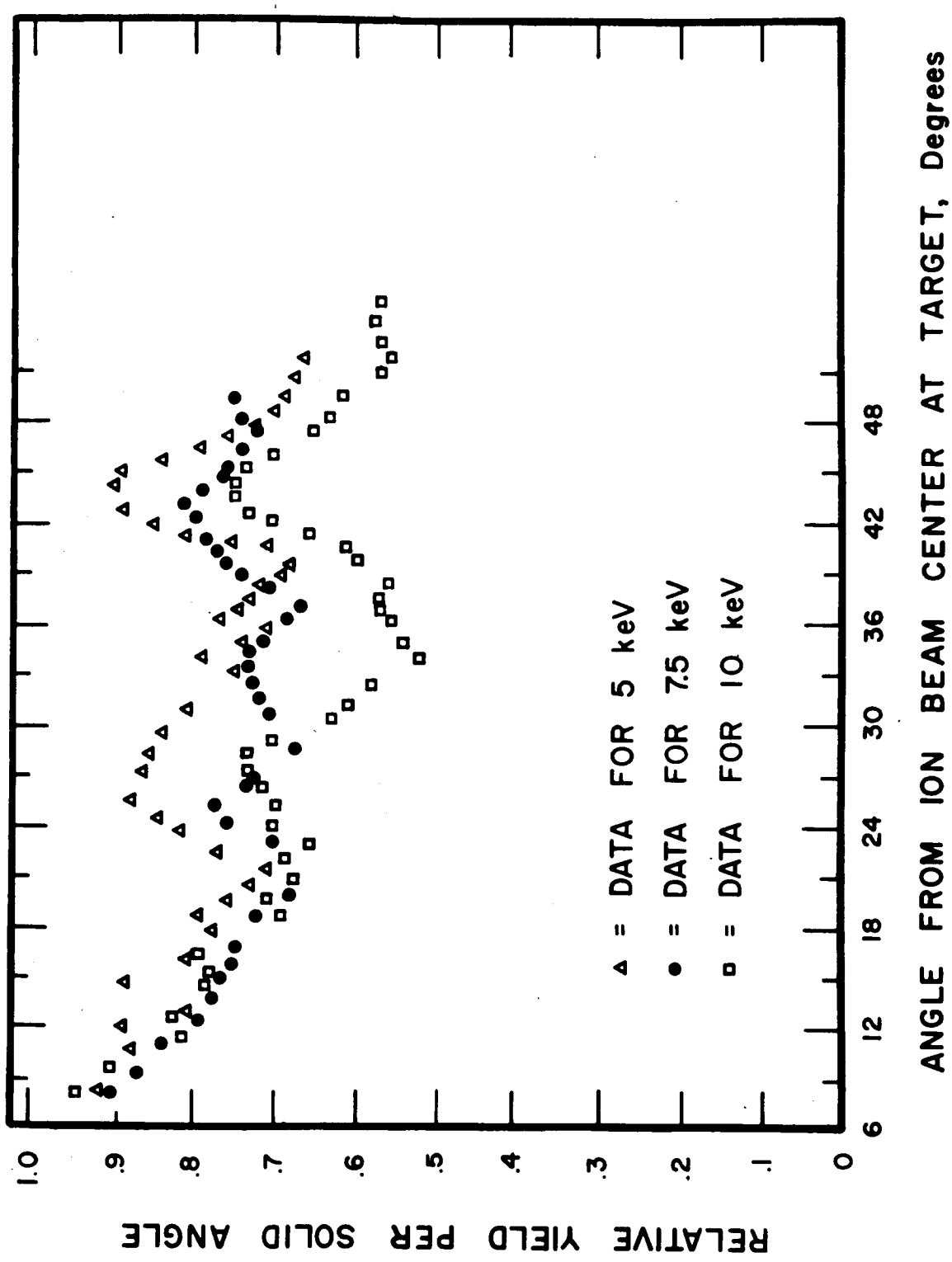

Figure 6-2: Relative sputtering yield in (001) plane for 5.0, 7.5, and 10 keV cesium ions incident on (001) face of aluminum single crystal.

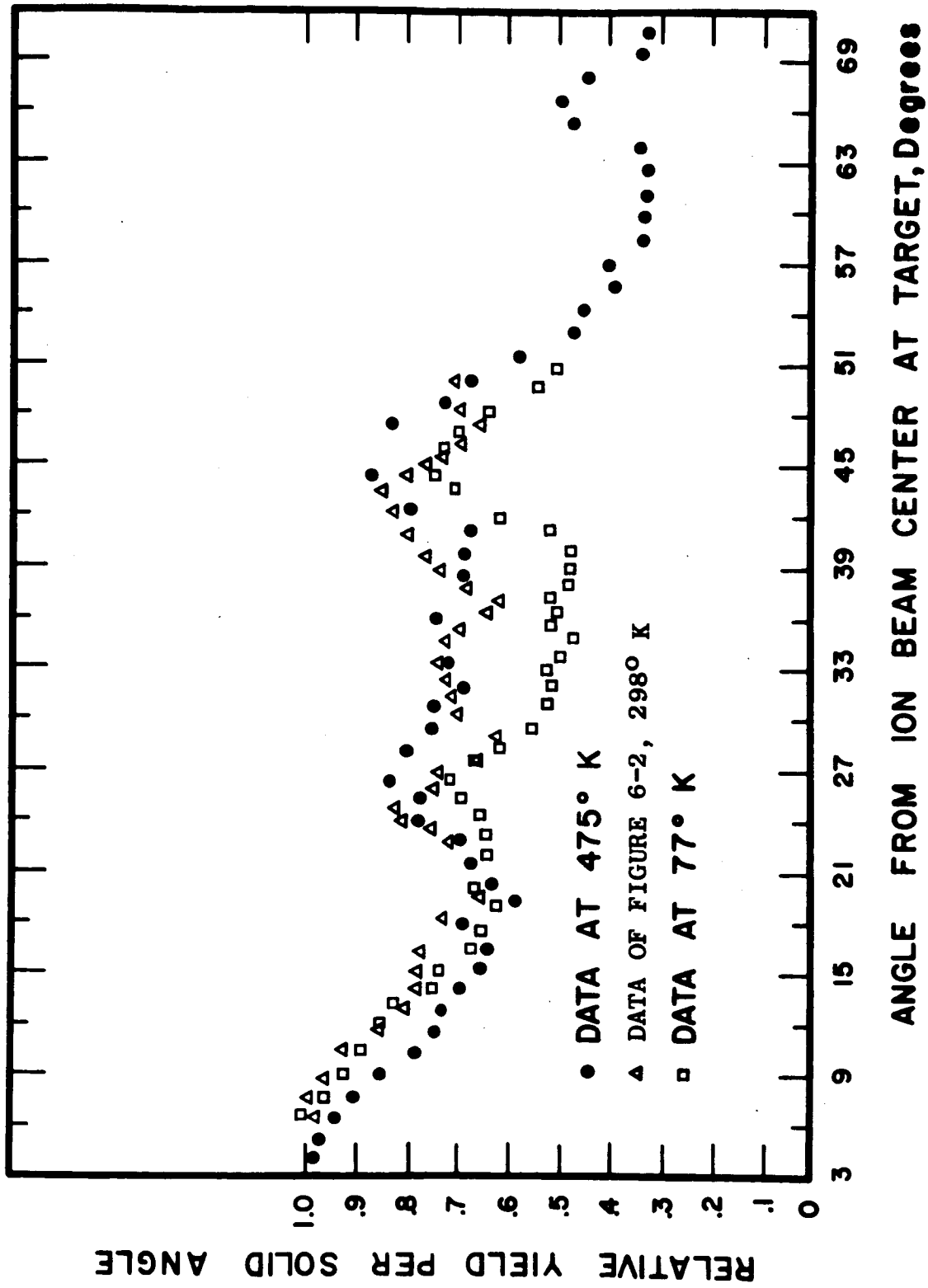

Figure 6-3: Relative sputtering yield in (001) plane for 7.5 keV cesium ions incident on (100) face of aluminum single crystal at 77°K, 298°K, and 475°K.

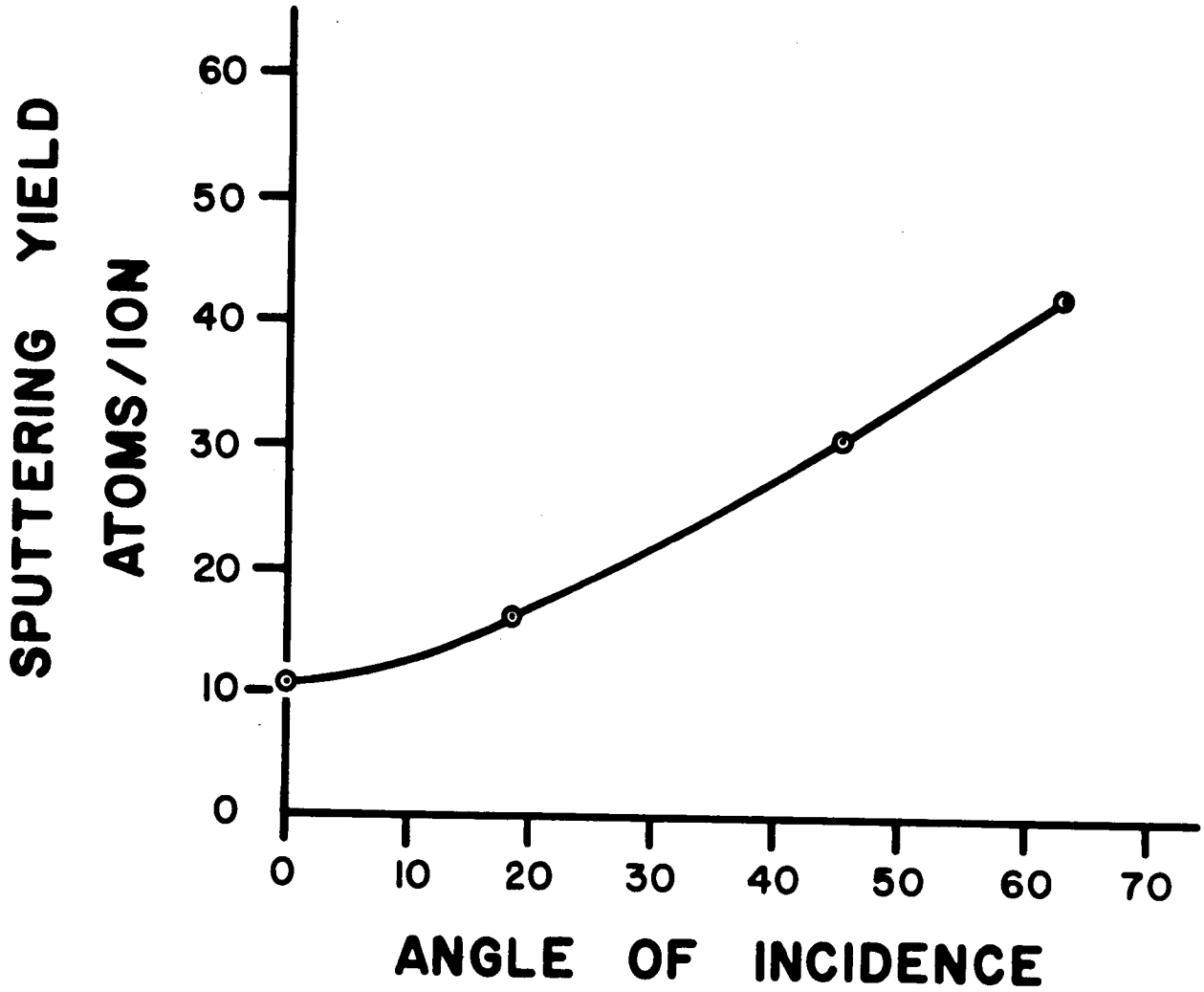

Figure 7-6: Sputtering yield dependence upon angle of incidence for 7.5-keV Hg^+-ions bombarding copper.

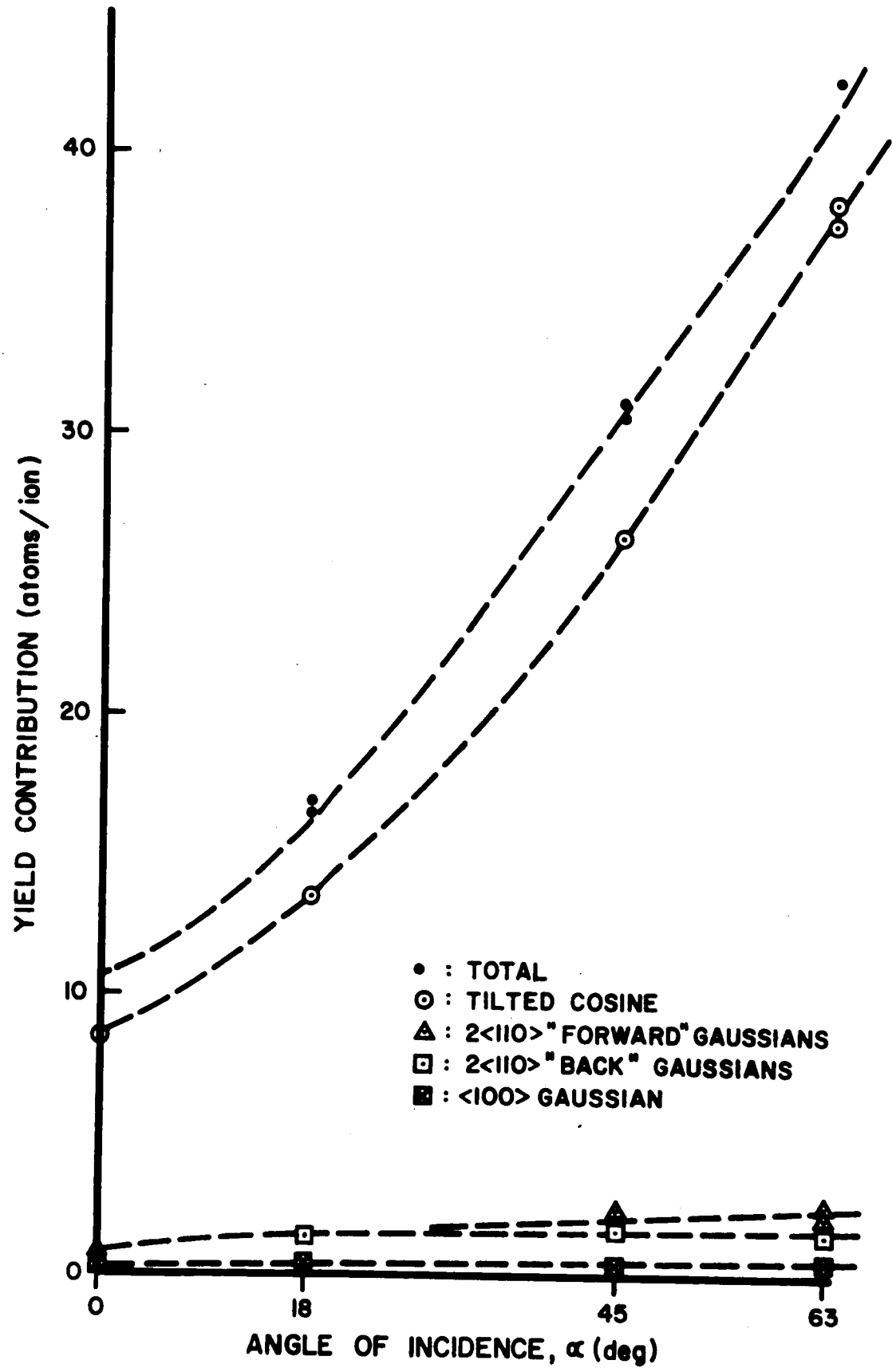

Figure 7-9: Absolute contributions to the sputtering yield of a (100) copper plane for obliquely incident, 7.5-keV Hg^+-ions.

Ion Energy keV	Target Temperature	Total Yield (Atoms/Ion)	$\frac{B_1}{2}$	$4B_2\sigma^2$	$\frac{B_1}{2} + 4B_2\sigma^2$	σ
1	77° K	2.2	.77	.17	.94	9.2°
2.5	"	5.4	.83	.13	.96	8.0°
5	"	6.3	.88	.14	1.02	8.1°
7.5	"	6.2	.94	.12	1.06	7.1°
10	"	6.0	.91	.13	1.04	7.1°
1	293° K	2.1	.75	.17	.92	9.7°
2.5	"	5.6	.78	.16	.94	9.6°
5	"	6.7	.92	.11	1.03	6.7°
7.5	"	5.9	.91	.11	1.02	7.1°
10	"	5.7	.89	.09	.98	7.1
1	473° K	2.1	.84	.18	1.02	9.4°
2.5	"	4.8	.92	.13	1.05	8.5°
5	"	6.8	1.00	.11	1.11	7.8°
7.5	"	6.0	.95	.11	1.06	8.0°
10	"	6.2	.99	.10	1.09	7.7°

Table 2-1: Tabulated values of adjustable constants in Eq. (1) as a function of incident ion energy and target temperature. It should be noted that $B_1/2$ is the relative emission in a cosine distribution while $4B_2\sigma^2$ is the relative emission in the preferred, close-packed directions.

TABLE 7-1

RESULTS OF FITTING THE NORMAL-INCIDENCE COPPER DATA TO THE ANALYTICAL FUNCTION, EQ. (7-1)

Ion Energy (keV)	Data	B_1	B_2	B_3 (deg.)	B_4 (deg.)	B_5 (deg.)	B_6	AAPD*	RMSD**
1.0	1	1.39	2.74	8.6	47.8	45.0	---	15.1	0.20
2.5	1	1.37	2.50	7.8	47.2	44.3	---	17.0	0.23
5.0	1	1.43	2.06	7.6	47.6	42.7	0.23	16.6	0.21
7.5	1	1.15	1.81	7.8	46.6	44.0	1.38	18.4	0.18
7.5	2	1.46	2.05	7.8	47.4	44.9	1.22	14.1	0.19
7.5	3	1.51	2.11	7.7	47.6	46.0	0.50	15.8	0.22
10.0	1	1.24	2.07	7.5	47.4	42.7	1.40	17.8	0.21

*AAPD - Average Absolute Percent Deviation

**RMSD - Root Mean Square Deviation

TABLE 7-2

RESULTS OF FITTING THE MOLYBDENUM DATA TO THE ANALYTICAL FUNCTION, EQ. (7-1)

Ion Energy (keV)	Temp (°K)	Data	B_1	B_2	B_3 (deg.)	B_4 (deg.)	B_5 (deg.)	B_6	AAPD*	RMSD**
1.0	300	1	1.12	1.06	14.3	55.5	46.1	--	10.4	0.13
2.5	300	1	1.38	0.62	11.5	54.6	52.5	--	9.3	0.11
5.0	300	1	1.41	0.46	9.8	56.8	44.8	1.05	7.5	0.08
7.5	300	1	1.48	0.39	10.2	56.6	48.6	1.30	8.7	0.12
7.5	300	2	1.30	0.30	8.6	55.3	48.8	1.96	8.1	0.08
7.5	95	1	1.30	0.36	10.2	58.7	50.9	1.34	9.0	0.10
7.5	480	1	1.29	0.36	7.7	57.8	48.3	2.54	10.1	0.10
10.0	300	1	1.46	0.40	7.8	58.1	46.0	2.96	6.5	0.08
10.0	300	2	1.24	0.35	9.4	57.1	47.5	3.03	12.1	0.11

*AAPD - Average Absolute Percent Deviation

**RMSD - Root Mean Square Deviation

TABLE 8-1

Interpolated values of the oxygen-K x-ray yield $I_T(E_o)$ from thick-target aluminum oxide and the oxygen K-shell x-ray production cross section $\sigma(E_o)$

E_o(keV)	$I_T(E_o)$(x rays/proton) (± 3%)	$\sigma(E_o)$(cm^2) (± 5%)
100	4.85×10^{-5}	8.25×10^{-23}
95	4.00×10^{-5}	7.00×10^{-23}
90	3.15×10^{-5}	5.90×10^{-23}
85	2.53×10^{-5}	4.95×10^{-23}
80	1.98×10^{-5}	4.02×10^{-23}
75	1.52×10^{-5}	3.28×10^{-23}
70	1.14×10^{-5}	2.55×10^{-23}
65	8.50×10^{-6}	2.00×10^{-23}
60	5.95×10^{-6}	1.50×10^{-23}
55	4.10×10^{-6}	1.10×10^{-23}
50	2.65×10^{-6}	7.65×10^{-24}
45	1.65×10^{-6}	5.10×10^{-24}
40	9.40×10^{-7}	3.40×10^{-24}
35	5.20×10^{-7}	1.85×10^{-24}
30	2.50×10^{-7}	1.00×10^{-24}
25	1.08×10^{-7}	4.75×10^{-25}
20	3.50×10^{-8}	1.95×10^{-25}

References

A1 Almen, O. and G. Bruce, Nucl. Instr. Methods 11, 279 (1961).

A2 Anderson, G.S., J. Appl. Phys. 34, 659 (1963).

A3 Anderson, G.S., G.K. Wehner, and H.J. Olin, J. Appl. Phys. 34, 2392 (1963).

A4 Akishin, A.I., S.S. Vasil'ev, and L.N. Isaev, Acad. Sci. USSR Bull. Phys. Sci. 26, 1379 (1962).

A5 Anderson, G.S., W.N. Mayer, and G.K. Wehner, J. Appl. Phys. 33, 2991 (1962).

A6 Anderson, G.S., J. Appl. Phys. 33, 2017 (1962).

A7 Ashmyanskii, R.A., M.B. Ben'Yaminovich, and V.I. Veksler, Soviet Phys. - Solid State 7, 1314 (1965).

A8 Allison, S.K. and S.D. Warshaw, Revs. Modern Phys. 25, 779 (1953).

B1 Behrndt, K.H., Physics of Thin Films, G. Hass and R.E. Thun, Eds. (Academic Press, Inc., New York, 1966), III, 8.

C1 Cooper, E.P, and M.M. Mills, North American Aviation Report No. SR-78, 1950 (unpublished).

C2 Coltman, R.R., T.H. Blewitt, C.E. Klabunde, and J.K. Redman, Bull. Amer. Phys. Soc. 4, 235 (1959).

C3 Carlston, C.E., G.D. Magnuson, A. Comeaux, and P. Mahadevan, Phys. Rev. 138, A759 (1965).

C4 Cunningham, R.L., and J. Ng-Yelim, J. Appl. Phys. 35, 2184 (1964).

C5 Covell, D.F., U.S. Naval Radiological Defense Laboratory, Mare Island, California, Tech. Report No. 288.

D1 Daley, H.L. and J. Perel, AIAA Paper No. 66-203.

D2 Davies, J.A., J. Friesen, and J.D. McIntyre, Can. J. Chem. 38, 1526 (1960).

References

F1 Similar results can be noted in argon-copper sputtering: J.M. Fluit, J. Kistemaker, and C. Snoek, Physica 30, 870 (1964).

G1 Gronlund, F.,and W.J. Moore, "Sputtering of silver by light ions with energies from 2 to 12 keV," J. Chem. Phys. 32, 1540-1545 (1960).

G2 Green, J.B., N. Thomas Olson, and H.P. Smith, Jr., J. Appl. Phys. 37, 4699 (1966).

G3 Grey, D.L., AEC Report HW-57903 (November 1958).

G4 Guentherschulze, A., and H. Betz, Z. Physik 108, 780 (1958).

H1 Harrison, Jr., D.E., J.P. Johnson, III, and N.S. Levy, Appl. Phys. Letters 8, 33 (1966).

H2 Hauffe, K., Oxidation of Metals (Plennum Press, New York, 1965), 405.

H3 Harris, L. J. Opt. Soc. Am. 45, 27 (1955).

H4 Hauser, U. and W. Kerler, Rev. Sci. Instr. 29, 380 (1958).

H5 Hass, G., J. Opt. Soc. Am. 39, 532 (1949).

J1 Jorgenson, G.V., and G.K. Wehner, J. Appl. Phys. 36, 2672 (1965).

K1 Kornelson, E.V., F. Brown, J.A. Davies, B.Domeij, and G. Piercy, "Penetration of heavy ions of keV energies into monocrystalline tungsten," Phys. Rev. 136, A849-A858 (1964).

K2 Kinchin, G.H. and M.W. Thompson, J. Nucl. Energy 6, 275 (1958).

K3 Koedam, M. and A. Hoogendoorn, Physica 26, 351 (1960).

K4 Khan, J.M., D.L. Potter, and R.D. Worley, J. Appl. Phys. 37, 564 (1966).

K5 Khan, J.M., D.L. Potter, and R.d. Worley, Phys. Rev. 139, 1735 (1965).

References

K6 Khan, J.M., D.L. Potter, R.D. Worley, and H.P. Smith, Jr., Phys. Rev. 148, 413 (1966).

L1 Lewis, J.E., and R.C. Plumb, Intern. J. Appl. Radiation and Isotopes, 1, 33 (1956).

M1 Magnuson, G.D., and C.E. Carlston, J. Appl. Phys. 34, 3267 (1963).

M2 Mark, Hans, and N. Thomas Olson, "Experiments in Modern Physics" (McGraw-Hill Book Company, New York, 1966).

M3 Molchanov, V.A., V.G. Tel'Kovskii, and V.M. Chicherov, Soviet Phys. - Doklady 6, 222 (1961).

M4 Model 400, Materials Analysis Company, Palo Alto, California.

M5 Molchanov, V.A., V.G. Tel'Kovskii, and V.M. Chicherov, Soviet Phys. - Doklady 6, 486 (1961).

M6 Merzbacher, E. and H.W. Lewis, "Enclclopedia of Physics," S. Flügge, Ed. (Springer-Verlag, Berlin, 1958), 34, 166.

M7 Moak, C.D., H.E. Banta, J.N. Thurston, J.W. Johnson, and R.F. King, Rev. Sci. Instr. 30, 694 (1959).

N1 Nelson, R.S. and M.W. Thompson, "Atomic collision sequences in crystals of copper, silver, and gold revealed by sputtering in energetic ion beams," Proc. Roy. Soc. 259A, 458-479 (1961).

N2,3 Nelson, R.S., M.W. Thompson, and H. Montgomery, "The influence of thermal vibration on fucused collision sequences," Phil. Mag. 7, 1385-1405 (1962).

N4 Nelson, R.S., Phil. Mag 8, 693 (1963).

N5 Northcliffe, L.C., Ann. Rev. Nuclear Sci. 13, 67 (1963).

O1 O'Brian, C.D., A. Lindner, and W.J. Moore, "Sputtering of silver by hydrogen ions," J. Chem. Phys. 29, 3-7 (1958).

References

P1 Patterson, H. and D.H. Tomlin, "Experiments by radioactive tracer methods on sputtering by rare-gas ions," Proc. Roy. Soc. 265A, 474-488 (1961).

R1 Ramer, C.E., M.A. Narasimham, H.K. Reynolds and J.C. Allred, J. Appl. Phys. 35, 1673 (1967).

S1 Snouse has complied a considerable amount of data taken at $\alpha = 0$, demonstrating that the Cu yield for bombardment along the [100] direction exceeds that along the [110] direction over a wide range of E. Hence, our data emphasized the importance of reducing the effective penetration (i.e., oblique incidence) since the yields of the two crystallographic directions are revered by bombarding the [100] direction at $\alpha = 0$ and the [110] directions at $\alpha \doteq 45°$.

S2 Seitz, F. and J.S. Koehler, Solid State Phys. 2, 404 (1956).

S3 Silsbee, R.H. J. Appl. Phys. 28, 1246 (1957).

S4 Sanders, J.B. and J.M. Fluit, Physica 30, 239 (1964).

S5 Snouse, T.W. and L.C. Haughney, J. Appl. Phys. 37, 700 (1966).

S6 Southern, A.L., W.R. Willis, and M.T. Robinson, ibid., 34, 153 (1963).

S7 Amster, H.J., and R.N. Schlaug, Ph.D. thesis by Schlaug, Department of Nuclear Engineering, University of California, Berkeley (1965).

S8 Stein, R.P., and F.C. Hurlbut, Phys. Rev. 123, 790 (1961).

T1 Tegart, W.J. McG., "Electrolytic and Chemical Polishing of Metals," (Pergamon Press, New York, 1959), 57.

V1 von Ardenne, M., Tabellen der Elektronenphysik, Ionenphysik und Übermikroskopie (Deutscher Verlag der Wissenschaften, Berlin, 1956), 544.

References

W1 Wehner, G.K., Advan. Electron. Electron Phys. 7, 239 (1955).

W2 Wehner, G.K., General Mills Rept. No. 1902 (1959).

W3 Wehner, G.K., G.S. Anderson, and C.E. KenKnight, Final Report, Contract No. AT(11-1)-722, (1966).

Y1 Yonts, O.C. and D.E. Harrison, "Surface cleaning by cathode sputtering," J. Appl. Phys. 31, 1583-1584 (1960).

Y2 Yurasova, V.E., and E.A. Murinson, Acad. Sci. USSR Brell, Phys. 26, 1470 (1962).

Y3 Yurasova, V.E., Soviet Phys. - Tech Phys. 3, 1806 (1958).

Y4 Yurasova, V.E., N.V. Pleshivtsev, and I.V. Orfanov, Soviet Phys. - JETP 37, 689 (1960).

Y5 Young, L., "Anodic Oxide Films," (Academic Press, Inc., New York, 1961), 212.

FINAL REPORT DISTRIBUTION LIST
Contract NAS 3-5743

Copies	Addressee
	National Aeronautics and Space Administration Washington, D. C. 20546
1	Attn: RNT/James Lazar
1	RNT/J. Mullin
1	RRS/R. R. Nash
1	RNT/G. W. Pfannebecker
	National Aeronautics and Space Administration Lewis Research Center 2100 Brookpark Road Cleveland, Ohio 44135
1	Attn: R. R. Nicholls, MS 54-3
1	Technical Information Div.
1	C. C. Conger, MS 54-1
4	H. R. Hunczak, MS 54-3
2	H. R. Kaufman, MS 301-1
2	J. Ferrante, MS 302-1
1	J. Eski, MS 54-2
1	Technology Utilization Office, MS 3-19
2	Library, MS 60-3
1	Reports Control Office, MS 5-5
1	W. Moeckel, MS 301-1
1	H. Kosmahl, MS 54-3
	Hughes Research Laboratory 3011 Malibu Canyon Road Malibu, California 93032
1	Attn: Dr. G. Brewer
1	Dr. H. Wiser
1	Dr. W. Elkhard
	Electro-Optical Systems, Inc. 125 North Vinedo Avenue Pasadena, California 91107
1	Attn: J. A. Walters
1	G. Sohl
1	Dr. D. B. Medved
	Litton Industries Surface Physics Department Minneapolis, Minnesota
1	Attn: Dr. G. K. Wehner
	General Dynamics/Astronautics P. O. Box 1128 San Diego, California 92112
1	Attn: Dr. D. Magnuson
	Field Emission Corporation 611 Third Street McMinnville, Oregon
1	Attn: Dr. L. W. Swanson
	General Electric Company Flight Propulsion Laboratory Evendale, Ohio
1	Attn: Dr. M. L. Bromberg
	Physics Technology Labs., Inc. 7841 El Cajon Boulevard
1	La Mesa, California
	Air Force Weapons Laboratory Kirtland Air Force Base, New Mexico 87117
1	Attn: WLIL
1	WLPC/Capt. C. F. Ellis
	TRW Inc. One Space Park Redondo Beach, California 90278
2	Attn: E. Cohen
	National Aeronautics and Space Administration Marshall Space Flight Center Huntsville, Alabama 35812
1	M-RP-DIR/E. Stuhlinger
	National Aeronautics and Space Administration Scientific and Technical Information Facility P. O. Box 33 College Park, Maryland 20740
6	Attn: NASA Rep./RQT-2448
	Commander Aeronautical Systems Division Wright-Patterson Air Force Base, Ohio 45433
1	WPAFP-AFAPL (APIE)

FINAL REPORT DISTRIBUTION LIST
Contract NAS 3-5743

Copies	Addressee
	National Aeronautics and Space Administration Ames Research Center Moffett Field, California 94035
1	Attn: Mr. T. W. Snouse
1	Library
	Varian Associates 435 Harbor Boulevard Belmont, California 94002
1	Attn: Technical Library
	Astro-Met Associates, Inc. 500 Glendale-Milford Road Cincinnati, Ohio 45215
1	Attn: J. W. Graham
	Princeton University Dept. of Aeronautical Engineering Princeton, New Jersey
1	Attn: Professor J. B. Venn
	Hiram College Department of Physics Hiram, Ohio
1	Attn: Professor L. Shaffer
	University of Missouri Materials Research Center Rolla, Missouri
1	Attn: J. R. Wolfe
	P. R. Mallory and Company, Inc. 3029 East Washington Street Indianapolis, Indiana 46206
1	Attn: Technical Librarian
	National Aeronautics and Space Administration Goddard Space Flight Center Greenbelt, Maryland 20771
	Attn: Mr. Jule Hirschfield, Radiation Effect Group
1	Space Power Technology
1	W. Isley, Code 623

Copies	Addressee
	Oak Ridge National Laboratory P. O. Box X Oak Ridge, Tennessee 37831
1	Attn: Dr. James R. Woodyard
	Oak Ridge National Laboratory P. O. Box 62 Oak Ridge, Tennessee 37831
1	Attn: Technical Information Service Ext.
	Boeing Radiation Effects Laboratory Boeing Company P. O. Box 3707 Seattle Washington 98124
1	Attn: Dr. Eric H. Hasseltine
	Denver Research Institution University of Denver University Park Denver, Colorado 80210
1	Attn: Professor Robert C. Amme
	National Aeronautics and Space Administration Langley Research Center Hampton, Virginia 23365
1	Attn: Library
1	M. Ellis, MS 160
	Jet Propulsion Laboratory 4800 Oak Grove Drive Pasadena, California 91103
1	Attn: Library
2	D. Kerrisk
	Colorado State University Fort Collins, Colorado 80521
2	Attn: Professor W. Mickelson
	Cornell Aeronautical Labs. Buffalo, New York 14221
1	Attn: D. Lockwood
1	A. S. Gilmour, Jr.

FINAL REPORT DISTRIBUTION LIST
Contract NAS 3-5743

Copies	Addressee
	Cast Institute of Technology 10900 Euclid Avenue Cleveland, Ohio 44106
1	Attn: Professor Eli Reshotko
	Kollsman Instrument Corporation 80-08 45th Avenue Elmhurst, New York 11373
1	Attn: Samuel Baig
	USAF Office of Scientific Research Washington, D. C. 20525
1	Attn: Dr. M. Slawsky
	J. T. Kotnik 16808 Westdale Avenue
1	Cleveland, Ohio 44135